International Journal of Engineering Research & Technology (IJERT)
ISSN: 2278-0181
Vol. 15 Issue 06 , June - 2026

Synthesis of Automatic Vibration Attenuation of a Vehicle: A Skyhook-PID Active Suspension Approach for a Half-Car Model

Ebenezer Kofi Frempong
Department of Mechanical Engineering
University of Mines and Technology (UMaT),
Tarkwa, Ghana

Derick Kumordzi
Department of Mechanical Engineering
University of Mines and Technology (UMaT),
Tarkwa, Ghana

Aloysius Polley
Department of Mechanical Engineering
University of Mines and Technology (UMaT),
Tarkwa, Ghana

Dr. Augustine Akuoko Kwarteng
Department of Mechanical Engineering
University of Mines and Technology (UMaT),
Tarkwa, Ghana

***Abstract*- This study develops an automatic vibration attenuation system for a light passenger vehicle to reduce pothole-induced loading and improve ride comfort. A four-degree-of-freedom half-car model was developed for a two thousand and nine Toyota Camry using parameters from SolidWorks computer-aided design and finite-element analysis. Road disturbances were modelled as haversine potholes of one-hundred-millimetre depth and three-hundred-millimetre width at speeds of twenty, forty, and sixty kilometres per hour. A skyhook proportional-integral-derivative controller was designed in MATLAB and Simulink with realistic actuator constraints. The active controller reduced root-mean-square body acceleration by seventeen to twenty-one per cent, pitch angle by thirty-six to fifty-four per cent, and settling time by approximately fifty per cent, with average actuator utilisation near seventy-two per cent. The results confirm that a skyhook-PID active suspension can effectively neutralise pothole-induced shock loading while improving ride comfort and reducing shock-absorber wear.**

Keywords: Active suspension; Half-car model; Skyhook control; PID controller; Pothole-induced vibration; Shock absorber

I. INTRODUCTION

A. Background and Motivation

The suspension system of a road vehicle is central to ride comfort, road holding and structural durability. Within it, the shock absorber dissipates the vibrational energy stored in the sprung mass and limits spring rebound, thereby controlling body oscillation [1]. Conventional passive shock absorbers, however, employ a single fixed damping characteristic and therefore cannot adapt to the highly variable shock intensities produced by potholes, ruts and other abrupt surface discontinuities conditions that accelerate component wear and degrade passenger comfort [2].

Recent work on semi-active and adaptive suspension technologies, particularly magnetorheological (MR) dampers and electronically controlled valves, shows that real-time adjustment of damping force in response to road-disturbance severity can substantially reduce body acceleration and peak suspension loads relative to passive systems [3]. Realising such adaptive control, however, depends on an accurate dynamic model that couples multi-degree-of-freedom vehicle motion with realistic shock-absorber behaviour and tyre–road interaction [4].

Reduced-order half-car and quarter-car models, as well as full multibody simulations, have all been used to predict natural frequencies, modal responses and shock forces; the validity of any given model nevertheless depends on whether it can represent the force–velocity and valve-dynamics behaviour that governs real shock-absorber response [5]. Field and simulation studies focused specifically on pothole impacts further show that pothole geometry (depth and width) and vehicle speed jointly determine the transmitted impulse and the resulting peak force, so

International Journal of Engineering Research & Technology (IJERT)
ISSN: 2278-0181
Vol. 15 Issue 06 , June - 2026

that mapping the required damping force as a function of these variables is essential for specifying a controller's operating range and gains [4]. Combining SolidWorks structural analysis with time-domain numerical simulation in MATLAB/Simulink is an effective means of quantifying these peak forces and of sizing a control system capable of preventing shock-absorber damage under worst-case road inputs.

The economic and safety case for this work is reinforced by field measurements showing that pothole impacts can generate vertical suspension loads many times larger than those experienced on routine, well-maintained pavement [6], and by South African field studies confirming that pothole-induced accelerations measured on in-service vehicles routinely exceed comfort and component-durability thresholds derived from controlled laboratory testing [7]. In markets where road maintenance budgets are constrained and pothole repair cycles are long, shock absorbers are consequently replaced more frequently than in well-maintained networks, and ride discomfort is a near-daily occurrence for both private motorists and commercial fleet operators. An automatic vibration-attenuation system capable of quantifying and counteracting these loads therefore has a direct, practical payoff beyond the academic interest of the control problem itself: extended component service life, reduced unplanned maintenance, and measurably improved comfort and safety margins for vehicles that must routinely operate on poorly maintained roads.

B. Problem Statement

Shock absorbers control vertical vibration and maintain vehicle stability over uneven road surfaces, yet many road networks particularly in developing economies are characterised by potholes, rough patches and sudden surface discontinuities that generate high-impact vertical loads. These abrupt inputs frequently exceed the damping capacity of conventional passive absorbers, producing excessive oscillation, reduced comfort, accelerated wear and, in many cases, premature failure [2].

The force transmitted to the shock absorber during a pothole strike depends on the interaction of several variables, including vehicle speed, pothole depth and width, mass distribution, tyre stiffness and suspension geometry; when these variables combine unfavourably for example, a deep pothole struck at high speed the resulting impact force can readily exceed the operating limits of a passive damper [4]. Because passive absorbers use a fixed damping coefficient, they cannot adjust in real time to protect the suspension from such unpredictable shocks [3]. While semi-active and adaptive technologies demonstrate that variable damping can substantially reduce peak loads, their successful design depends on accurately determining (i) the damping force required at different driving speeds on rough roads, (ii) the effect of pothole dimensions on shock-absorber loading, (iii) the total force transmitted during an impact event, and (iv) the maximum damping force needed to prevent shock-absorber damage [1], [5], [8].

Existing literature does not provide a unified, quantitative framework that combines these factors for real-time vibration attenuation in light vehicles, leaving the actual damping demand required to protect suspension components on irregular roads inadequately characterised. This study addresses that gap by developing a mathematical and simulation-based framework that determines the forces acting on a vehicle shock absorber under realistic operating conditions and identifies the damping force required to attenuate sudden pothole-induced shocks, forming the basis for an automatic vibration attenuation system for light vehicles.

The practical consequence of this gap is that suspension and component engineers currently lack a repeatable, physically traceable basis for specifying the damping-force envelope an active or semi-active system must deliver for a given vehicle class and road-roughness profile. Published design guidance tends either to report aggregate ride-comfort outcomes without the underlying force data needed to size an actuator, or to derive that force data from generic, non-vehicle-specific parameters that cannot be directly mapped onto a particular production vehicle. Closing this gap requires three things simultaneously: a dynamic model detailed enough to capture the front-rear pitch coupling that dominates pothole response (Section II-C), a parameter set traceable to an actual vehicle's geometry and structural properties rather than to assumed or generic values (Section III-C), and a control law whose force, bandwidth and slew-rate demands can be checked directly against realistic actuator hardware (Section III-L). The methodology developed in Section III is structured explicitly around meeting all three conditions together, rather than treating model fidelity, parameter traceability and hardware feasibility as separate concerns.

C. Research Questions

Five research questions guide this study. (i) What levels of damping force are required to effectively control the vertical vibrations of a light vehicle operating at different speeds on rough, pothole-ridden roads? (ii) How do pothole characteristics specifically depth and width affect the magnitude of shock loads transmitted to the vehicle's shock absorber during sudden impacts? (iii) What is the total dynamic force acting on the shock absorber when the vehicle encounters a pothole of a given

International Journal of Engineering Research & Technology (IJERT)
ISSN: 2278-0181
Vol. 15 Issue 06 , June - 2026

geometry at a specified speed? (iv) What is the maximum damping force needed to prevent shock-absorber damage under worst-case shock conditions commonly experienced on irregular road surfaces? (v) How can a mathematical and simulation-based framework be developed to accurately predict shock-absorber forces and support the design of an automatic vibration-attenuation system for light vehicles? Together, these questions define the damping-force envelope that an automatic vibration-attenuation system must cover, and the methodology and results presented in Sections III and IV answer each of them in turn.

D. Aim, Objectives and Scope

The aim of this work is to develop an automatic vibration attenuation framework that determines the damping requirements of, and reduces shock-induced damage in, a light-vehicle suspension system operating on rough road surfaces. The specific objectives are to (i) determine the damping forces required by a light vehicle travelling at varying speeds on pothole-ridden roads, (ii) analyse the influence of pothole geometry on the resulting shock load, and (iii) model the dynamic behaviour of the suspension system in MATLAB/Simulink in order to establish the maximum damping force necessary to neutralise sudden shock loads.

The scope of the work is confined to the numerical modelling and analysis of vibration-attenuation requirements for a half-car suspension system incorporating body bounce, pitch motion and wheel-hop dynamics. MATLAB/Simulink is used to simulate system behaviour under varying pothole geometries and vehicle speeds, while SolidWorks CAD and finite-element analysis (FEA) provide the structural and inertial parameters. Performance evaluation is limited to the total force transmitted to the shock absorber, the damping force required under defined impact conditions, and the maximum damping force necessary to prevent shock-absorber damage. The study is strictly computational and analytical: physical prototyping, real-vehicle experiments, shock-absorber material testing, and detailed computational-fluid-dynamics modelling of damper internals fall outside its scope.

E. Significance and Contribution

This study contributes to the literature reviewed in Section II in three specific ways. First, it provides a complete, traceable parameter set for a 4-DOF half-car model derived directly from the CAD geometry and finite-element analysis of a named reference vehicle (the 2009 Toyota Camry) rather than from generic or assumed vehicle data, allowing every stiffness, damping and inertial value used in the simulation to be checked against its source. Second, it explicitly targets pothole geometry and vehicle speeds representative of West African urban and arterial road networks, an operating envelope that is comparatively under-represented in the suspension-control literature reviewed in Section II-I. Third, it reports actuator-force demand alongside ride-comfort and stability metrics, so that the proposed skyhook-PID controller is evaluated not only on its vibration-attenuation performance but also on its practical feasibility within the force, bandwidth and slew-rate envelope of commercially realistic hydraulic servo hardware. Taken together, these contributions extend the half-car/skyhook-PID literature from a largely generic, parameter-agnostic treatment toward a reproducible, vehicle-specific and hardware-aware design methodology that other researchers and practising engineers can adapt to different reference vehicles or road conditions.

F. Methods and Facilities Used

The methods applied in this study comprise a structured review of relevant literature; parameter extraction using SolidWorks CAD and finite-element analysis; mathematical derivation of the equations of motion via the Newton-Euler method; design and tuning of a PID controller in MATLAB/Simulink; and evaluation of the resulting actuator force and thermal-management implications. The principal facilities used were the University of Mines and Technology (UMaT) computing and modelling laboratories, together with SolidWorks and MATLAB/Simulink software licences, supplemented by field observation of representative pothole conditions on local road networks.

G. Paper Organisation

The remainder of this paper is organised as follows. Section II reviews the literature on vehicle suspension systems, shock-absorber theory, road-profile and pothole modelling, and semi-active/active damping technologies, concluding with the research gaps this study addresses. Section III presents the methodology, including model selection, CAD/FEA parameter extraction, derivation of the equations of motion, the road-disturbance model, the Simulink architecture and the skyhook-PID controller design. Section IV reports and discusses the simulation results, covering time-domain response, ride comfort, pitch attenuation, actuator-force utilisation and validation against ISO 2631 [9] and prior studies. Section V concludes the paper and outlines recommendations for future work.

II. LITERATURE REVIEW

Vehicle vibration control is a long-standing concern in automotive engineering because it directly affects comfort, safety and component durability [10]. Road irregularities, tyre non-

International Journal of Engineering Research & Technology (IJERT)
ISSN: 2278-0181
Vol. 15 Issue 06 , June - 2026

uniformity and engine excitation all transmit vibration into the vehicle body, causing passenger discomfort, driver fatigue and accelerated component wear [11]. Passive suspension systems remain attractive for their simplicity and low cost, but their fixed damping characteristic is a fundamental compromise that cannot perform optimally across the full range of driving conditions and speeds [12]; this limitation has driven sustained research interest in semi-active and active vibration-control strategies that use sensors, actuators and control algorithms to continuously adjust damping in real time [13], [14]. This section reviews suspension fundamentals, shock-absorber theory, vehicle dynamics models, road and pothole modelling, semi-active and active damping technologies, and the simulation tools used to study them, before identifying the gaps that motivate the present study, with particular attention to materials such as magnetorheological (MR) fluids and the computing techniques expected to shape the next generation of adaptive vehicle dynamics.

A. Vehicle Suspension Fundamentals

A vehicle suspension system supports the vehicle's weight, maintains continuous tyre–road contact, and isolates the sprung mass (the passenger cabin) from road unevenness [15]. It comprises three principal components: springs, dampers (shock absorbers), and linkages. Springs are elastic elements typically helical coil or air springs that store the vehicle's static load and absorb the initial energy of a road impulse [16], while dampers manage and dissipate the oscillation that the spring would otherwise sustain, which is essential for stability and safety [11]. Fig. 1 illustrates a representative vehicle suspension assembly and its constituent parts. Traditionally, suspension behaviour is analysed using simplified mathematical representations rather than the full vehicle structure; the most common starting point is the quarter-car model, a two-degree-of-freedom system representing a single wheel station, which is widely used because it efficiently predicts the main characteristics of ride comfort and road holding [17]. Studies concerned with body rotation pitching for front-to-rear motion, or rolling for side-to-side motion instead require half-car or full-car models, discussed further in Section II-C.

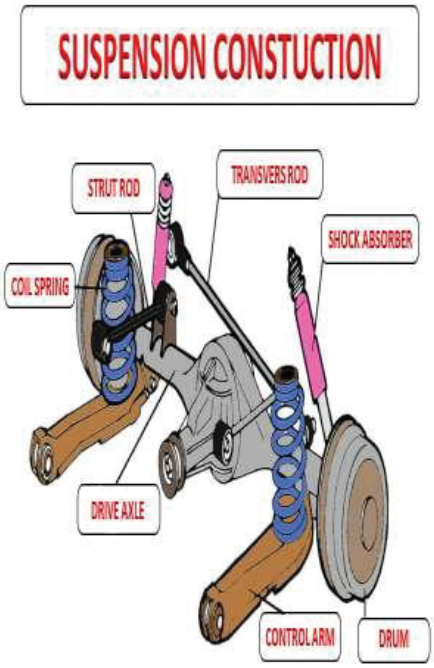

Fig. 1. Vehicle suspension system and its components [11].

1) Historical Evolution of Suspension Systems: The history of vehicle suspension is a progression from simple mechanical hardware to increasingly capable electronically controlled systems, driven by the inherent conflict between ride comfort and handling stability [12]. The earliest passive suspension systems, composed of steel springs and hydraulic dampers, remain the most common owing to their simplicity and low cost [18], but the limitations of a fixed-setting system became apparent as road conditions and performance expectations grew: a passive system simply cannot deliver both a smooth ride and sharp handling at once [11]. This inherent compromise motivated the development of adaptive technologies. The first significant step toward automation was the semi-active suspension, which emerged around the 1970s with controllable dampers notably those using magnetorheological (MR) fluids capable of rapidly varying damping force in real time without adding energy to the system [18], [19]. This was a critical advance because it offered a flexible performance trade-off at comparatively low power and complexity [20]. The fully active suspension, pioneered later in the twentieth century, instead uses powerful actuators to actively add or remove energy from the suspension, offering the greatest potential for controlling roll, pitch and bounce simultaneously [13].

2) Role and Function of Shock Absorbers: A shock absorber's primary role is not to bear the vehicle's weight that is the spring's function but to dampen the continuous oscillation of the spring after a bump is encountered [21], [22]. Damping is

International Journal of Engineering Research & Technology (IJERT)
ISSN: 2278-0181
Vol. 15 Issue 06 , June - 2026

achieved by converting the kinetic energy of suspension motion into thermal energy: mechanically, the shock absorber is essentially a piston moving within a tube of hydraulic fluid, and as the suspension compresses or rebounds the piston forces fluid through small restrictive orifices, generating a resisting force that quickly arrests excessive spring motion [21], [23]. The resulting functional outcome maintaining continuous, reliable tyre–road contact is essential for safe steering, stable handling and effective braking [24].

The three suspension classes introduced above passive, semi-active and active differ systematically in cost, complexity, power demand and achievable ride comfort, as summarised in Table 1. This trade-off space frames the control-strategy choice developed later in this paper (Section III-J): the present study's skyhook-PID controller occupies the active category in terms of force authority, while deliberately retaining the comparative simplicity and physical interpretability more typical of the semi-active control literature.

TABLE 1. COMPARISON OF PASSIVE, SEMI-ACTIVE AND ACTIVE SUSPENSION SYSTEMS [13], [18], [25].

Feature	Passive	Semi-Active	Active
External power required	No	Low	High
Damping adjustability	Fixed	Continuous	Continuous
Energy added to system	No	No (dissipates only)	Yes
Controller complexity	None	Moderate	High
Cost	Low	Moderate	High
Power consumption	0 W	25–50 W	1,000–3,000 W
Ride comfort, rough roads	Poor	Good	Excellent
Typical application	Economy vehicles	Mid-range vehicles	Luxury vehicles

B. Mechanical Characteristics of Springs and Dampers

The automatic control of vehicle vibration relies fundamentally on the mechanical characteristics of its springs and dampers [10]. A spring's principal characteristic is its stiffness, or spring rate k, which for a simple coil spring follows Hooke's law, relating spring force Fs to displacement x as Fs = kx [18], [26]. Modern systems increasingly employ non-linear springs, such as air springs, whose stiffness varies dynamically with load and compression, which is useful for automatic ride-height levelling. A damper's key characteristic is its damping coefficient c, relating damping force Fd to piston velocity v as Fd = cv [26]. Passive dampers typically exhibit a fixed, asymmetric force–velocity relationship, while in magnetorheological dampers the coefficient c can itself be varied electrically by adjusting the applied magnetic field, which is the mechanism that enables high-performance semi-active vibration attenuation [18].

1) Non-Linear Force–Velocity Characteristics: While simplified analysis often treats damping force as linearly proportional to piston velocity, real dampers exhibit pronounced non-linear behaviour arising from internal hydraulic effects such as fluid inertia and pressure loss across the internal orifices [18], [27]. Many dampers are deliberately designed to be digressive, producing high damping force at low piston speed (minimising chassis movement on small inputs) with a shallower force increase at high speed (preventing harshness on large bumps such as potholes) [27]. Capturing this velocity-dependent, non-symmetrical behaviour using models such as the Bouc-Wen formulation is a necessary foundation for control strategies that exploit these characteristics for optimal attenuation [28].

2) Influence of Damper Hysteresis: Damping force depends not only on instantaneous velocity but also on the recent motion history, an effect known as hysteresis, primarily caused by friction between the piston seals and cylinder wall, the dynamic behaviour of fluid flow through the orifices, and component elasticity [29], [30]. While the damper's main purpose is to dissipate energy smoothly, excessive friction-induced hysteresis can introduce unwanted high-frequency vibration, or “harshness”, particularly noticeable during small, rapid road inputs; robust control design therefore requires both modelling and compensation of this hysteresis to ensure smooth, predictable vibration reduction [31].

3) Influence of Mass Distribution: The distribution of a vehicle's total mass between front and rear axles, and the location of its centre of gravity, profoundly affects vibration behaviour and the effectiveness of any attenuation system [28], [32]. Changes in loading additional passengers or cargo alter the centre of gravity and the sprung mass carried by each axle, changing the natural frequencies of pitch and bounce; if not actively compensated, this can shift resonance to lower speeds and increase vibration intensity regardless of the specific load configuration [19].

C. Vehicle Dynamics Models

Effective controller development depends on selecting an appropriate mathematical representation of the vehicle [26]. The quarter-car model, a two-degree-of-freedom (2-DOF) representation of a single wheel station and a quarter of the body mass, is widely used for preliminary

International Journal of Engineering Research & Technology (IJERT)
ISSN: 2278-0181
Vol. 15 Issue 06 , June - 2026

control design because it efficiently captures the dominant vertical ride-comfort and road-holding dynamics [27]. The half-car model extends this to four degrees of freedom by representing the vehicle along its length, capturing both vertical bounce and pitch rotation, and is therefore well suited to studying longitudinal disturbances such as those produced by braking, acceleration, or as in the present study a pothole struck sequentially by the front and rear wheels [17], [20]. Fig. 2 shows a representative half-car model with its principal coordinates.

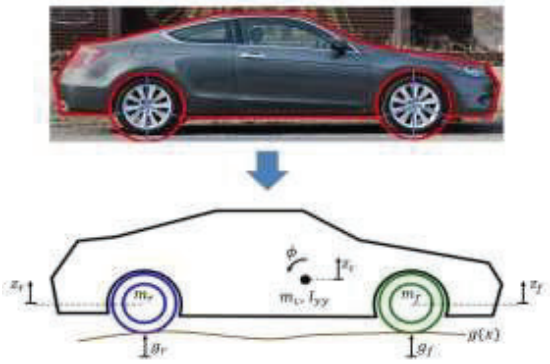

Fig. 2. Representative half-car model: body bounce (xc), pitch (φ) and front/rear wheel-hop coordinates [17].

The full-car model is the most comprehensive of the three, incorporating all four wheels and thereby allowing analysis of roll as well as bounce and pitch, at a correspondingly higher computational cost [26]. Table 2 summarises the key differences between the three model classes; the half-car model's combination of front-rear coupling and moderate computational cost makes it the natural choice for studies, such as this one, that are specifically concerned with pothole events struck asymmetrically by the front and rear wheels.

TABLE 2. COMPARISON OF QUARTER-CAR, HALF-CAR AND FULL-CAR SUSPENSION MODELS [17], [20], [26].

Feature	Quarter-Car	Half-Car	Full-Car
Degrees of freedom	2	4	7 or more
Body bounce captured	Yes	Yes	Yes
Body pitch captured	No	Yes	Yes
Body roll captured	No	No	Yes
Front-rear coupling	No	Yes	Yes
Left-right coupling	No	No	Yes
Computational cost	Low	Moderate	High
Suitable for pothole analysis	Limited	Yes	Yes

D. Shock-Absorber Theory and Modelling

The theoretical basis of shock-absorber operation is viscous damping: kinetic energy from suspension motion is converted to heat as hydraulic fluid is forced through restrictive orifices in the piston [27]. Because friction and hysteresis make this process inherently non-linear, simple linear models are insufficient for high-fidelity control design; the Bouc-Wen model and its extensions are widely adopted because they capture the coupled damping, stiffness and hysteresis-loop behaviour characteristic of controllable dampers [27].

1) Compression and Rebound Behaviour: A shock absorber is deliberately designed with different damping forces in compression and rebound an asymmetry engineered to balance ride comfort against handling stability [11], [18]. During compression, when the suspension absorbs a road input, damping force is kept relatively low so the sprung mass can absorb energy comfortably; during rebound, when the spring pushes the sprung mass back toward equilibrium, damping force is significantly higher in order to arrest upward momentum quickly and prevent excessive oscillation or "float", both of which are important for stability and safety [11].

2) Heat Generation, Fade and Wear: Because damping inherently converts kinetic energy into heat, thermal effects are a constant feature of shock-absorber operation [14]. The quantity of heat generated relates directly to damping force and the distance over which it acts [24], and as fluid temperature rises its viscosity and hence the effective damping coefficient falls, a phenomenon known as damping fade that reduces absorber effectiveness during sustained operation [14]. This thermal instability complicates control design because the effective damping 'constant' c becomes, in practice, a slowly time-varying parameter dependent on recent operating history; conversely, very low ambient temperatures can excessively raise fluid viscosity, impairing initial ride comfort. Mechanically, shock absorbers are also subject to well-characterised wear and failure modes: internal friction between piston, rod and seals gradually degrades the sealing components, leading to oil leakage ("weeping") and consequent loss of damping force; loss of internal gas charge in gas-pressurised dampers can cause cavitation, severely disrupting smooth operation; and repeated high-velocity impacts can cause structural failure of the piston rod or internal valves [33], [34].

3) Valve Dynamics and Flow Characteristics: The damping force generated by a shock absorber is fundamentally governed by valve dynamics and the resulting fluid-flow characteristics within the cylinder [14]. As the piston moves, fluid is forced through small, shaped orifices controlled by a piston

International Journal of Engineering Research & Technology (IJERT)
ISSN: 2278-0181
Vol. 15 Issue 06 , June - 2026

valve (regulating flow above the piston) and, in twin-tube designs, a base valve (regulating flow into the reserve tube) [34]. The pressure drop across these valves is the direct source of damping force and depends strongly on orifice geometry and fluid velocity. Passive dampers use spring-loaded shims to produce the digressive, asymmetric force-velocity curves discussed in Section II-B1, whereas semi-active systems use controllable solenoid or magnetorheological valves to instantaneously adjust the effective orifice area, enabling the variable damping exploited by the control strategies reviewed in Section II-G.

E. Road Profile and Pothole Modelling

Potholes represent a localised, high-intensity disturbance that generates a sudden, large-amplitude, short-duration velocity input at the wheel, producing transient body accelerations and a risk of momentary loss of tyre contact [14], [35]. General road roughness, by contrast, is usually modelled as a stochastic process characterised by its Power Spectral Density (PSD), which allows roads to be classified from very smooth (Class A) to very poor (Class E) [14], [35]. Advanced systems with road-scanning or "preview" sensing aim to detect such disturbances in advance, allowing the controller to pre-adjust damping before the wheel reaches the pothole a strategy this study's recommendations (Section V-B) identify as a promising extension. Fig. 3 and Fig. 4 show, respectively, a representative section of severely pot-holed urban road and the irregular, unpaved road conditions characteristic of many West African networks, while Fig. 5 shows a tyre in direct contact with a pothole edge.

Fig. 3. Representative urban road surface with multiple potholes [35].

1) Road Irregularity and Roughness: Road irregularity, or roughness, is the deviation of the road surface from a perfectly flat plane and is the fundamental source of vehicle vibration [35]. Because this irregularity is generally modelled as a stochastic rather than deterministic process, its exact height at any point cannot be predicted, though its statistical properties quantified through the PSD are consistent and allow classification of road quality for simulation purposes [14], [18].

Fig. 4. Irregular, pothole-affected road conditions typical of West African urban networks.

2) Influence of Pothole Shape on Impact Loads: The geometric shape of a pothole strongly influences the magnitude and profile of the resulting impact load [36]. A pothole with sharp, near-vertical edges acts as a sudden, severe impulse: as the tyre meets the near-vertical entry edge, a high-frequency, large-magnitude force is generated almost instantaneously, maximising unsprung-mass acceleration and potentially causing tyre lift-off [14]. A pothole with sloping or rounded edges instead produces a more gradual force profile, with a lower peak and longer duration, resulting in less severe vibration. Knowing the likely severity associated with a given pothole shape allows a control algorithm to pre-emptively stiffen the damper for sharp impacts (to prevent bottoming out) or soften it for rounded impacts (to maximise energy absorption), optimising the trade-off between comfort and handling [14].

3) Vehicle Speed Effects on Pothole-Induced Shocks: Vehicle speed is one of the most critical factors determining the severity of a pothole-induced shock [36]. As speed increases, the time available for the wheel to traverse a pothole of fixed geometry decreases, raising the rate of change of wheel displacement and hence the peak impact force on the suspension and tyre, while reducing ride comfort through greater unsprung-mass acceleration [14]. For a fixed pothole geometry, the excitation frequency applied to the suspension is directly proportional to vehicle speed; at high speed this can push the suspension into frequency ranges where its components are less effective at damping, occasionally producing severe wheel hop [18].

International Journal of Engineering Research & Technology (IJERT)
ISSN: 2278-0181
Vol. 15 Issue 06 , June - 2026

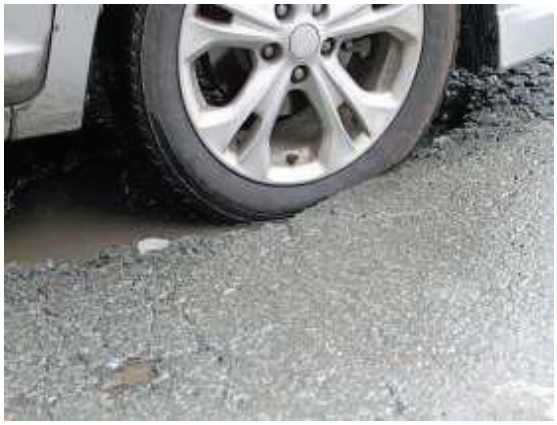

Fig. 5. Vehicle tyre in contact with a pothole on a rough road surface [19].

4) Road–Suspension–Tyre Impact Mechanics: The tyre is the primary element mediating dynamic interaction between the road surface and the suspension, acting as a flexible interface whose mechanics are governed by its vertical stiffness Kt and internal damping [18], [19]. During high-speed impacts, tyre deformation dissipates a significant portion of the shock load, reducing the force initially transmitted to the suspension, though the tyre's inherent stiffness also contributes high-frequency content to the vibration felt by occupants [14]. A key concern is wheel hop, a condition in which large transient forces cause the unsprung mass to momentarily lose road contact, severely degrading steering and braking performance and requiring rapid intervention from any active or semi-active suspension system [18].

F. Vehicle Dynamic Response Analysis

Dynamic-response analysis of a vehicle suspension is conventionally framed around three performance objectives: ride comfort, measured via sprung-mass RMS acceleration, for which lower values indicate better isolation of the passenger compartment; road holding, measured via dynamic tyre-load variation, for which minimising variation ensures constant tyre contact for steering and braking safety; and suspension-deflection limits, which prevent the system from “bottoming out” against its mechanical stops, avoiding both discomfort and damage [11], [14].

1) Natural Frequencies and Mode Shapes: Suspension behaviour is fundamentally defined by its natural frequencies and corresponding mode shapes, which dictate the frequencies at which the structure resonates when excited [18]. Two characteristic bands are of particular interest: the sprung-mass natural frequency (typically 1–2 Hz), corresponding to the primary body motions of bounce, pitch and roll, where minimising resonance is paramount for ride comfort [11]; and the unsprung-mass natural frequency (typically 10–15 Hz), corresponding to wheel/axle motion, where minimising resonance is critical for road holding and the prevention of wheel hop [14].

2) Transient Shock Response and Load Transfer: Encountering a pothole generates a distinct transient shock response characterised by a sudden, non-periodic oscillation that decays over a few seconds, differing significantly from the steady-state vibration produced by continuous road roughness; the rapid, large-amplitude displacement excites both the low-frequency sprung-mass mode and the high-frequency unsprung-mass mode simultaneously [14], [36]. Such events also redistribute load dynamically among the wheels: when both front wheels strike a pothole together, the rapid downward acceleration followed by rebound produces a transient nose-dive and recovery (longitudinal load transfer affecting braking stability), while a disturbance striking only one side of the vehicle induces a transient roll moment (lateral load transfer affecting steering feel) [11], [18]. In the half-car geometry adopted for this study, only the longitudinal (pitch-inducing) case is represented, consistent with the model's deliberate exclusion of roll dynamics (Section II-C).

G. Semi-Active and Adaptive Damping Strategies

Semi-active systems modulate damping force in response to sensor feedback but, unlike active systems, only dissipate energy rather than adding it; their core components are a controllable damper and an electronic control unit [18].

1) Magnetorheological (MR) Dampers: MR dampers use a fluid containing micron-sized magnetic particles whose viscosity changes almost instantaneously when a magnetic field is applied via a solenoid coil, enabling continuous, fast adjustment of damping force that is highly effective for rapid transient events such as potholes [34].

2) Electromagnetic and Solenoid-Valve Dampers: These devices use proportional solenoid valves to restrict conventional hydraulic fluid flow through the piston orifices, offering a simpler, lower-cost alternative to MR fluids, but typically with a slower response time and a narrower range of force variability [11].

3) Continuous Damping Control: Adaptive damping more broadly refers to systems whose damping characteristic is varied automatically, often in discrete steps or according to pre-defined control maps, rather than continuously; Continuous Damping Control (CDC) is a more sophisticated form that uses continuously variable proportional solenoid valves to provide a wide, stepless range of damping rates [18].

International Journal of Engineering Research & Technology (IJERT)
ISSN: 2278-0181
Vol. 15 Issue 06 , June - 2026

4) Skyhook, Ground-Hook and Hybrid Control: The dominant control strategy for semi-active and active systems of this kind is skyhook control. The intuition behind it is that of an imaginary damper connecting the vehicle body to a fixed point in the sky: since no such hook can exist physically, a controllable damper is instead commanded to act as if it did stiffening when the body moves away from its equilibrium position and softening as it returns [14], [37]. Ground-hook control applies the analogous logic to the wheel rather than the body: the damper is controlled to limit wheel bounce, improving grip for steering and braking, though without the comfort benefit of skyhook control [27]. Hybrid control blends the two strategies through a mixing ratio, favouring comfort when the ratio is high and road grip when it is low, allowing a single controller to balance both objectives [18]. The present study adopts a pure skyhook strategy (Section III-K), prioritising ride comfort consistent with the project's central aim of protecting the shock absorber and improving passenger experience.

H. Simulation Methods and Analytical Tools

1) MATLAB/Simulink Modelling: MATLAB/Simulink is the standard platform for vehicle-suspension analysis, representing the governing equations of motion as interconnected blocks of masses, springs, dampers and external forces and enabling rapid prototyping of control algorithms with direct visualisation of transient response [38]. A typical half-car Simulink implementation uses integrator chains to convert accelerations to velocities and then displacements for each degree of freedom, with road input generated via signal-builder or MATLAB function blocks; a haversine pulse is a common and effective representation of a pothole [39]. Reported Simulink-based half-car models accurately reproduce body-bounce, pitch-acceleration and tyre-deflection behaviour under realistic road conditions [40].

2) Finite Element Analysis: Finite-element analysis (FEA) complements system-level simulation by resolving how the forces predicted by MATLAB/Simulink translate into local stresses, strains and deflections within individual suspension components [41]. For suspension springs, FEA typically uses helical geometry models with defined wire diameter, coil pitch and active-coil count, with a vertical compressive load corresponding to the static load carried at that corner of the vehicle; the resulting stress distribution indicates whether the spring is likely to yield or fatigue under dynamic loading [42]. A well-constructed FEA model uses tetrahedral meshing with local refinement at stress-concentration points, allowing failure-prone regions to be identified ahead of any physical prototyping [43].

It is worth noting that MATLAB/Simulink is not the only platform used for this class of problem in the literature: full multibody dynamics packages such as ADAMS, and dedicated vehicle-dynamics environments such as CarSim, are also widely reported, particularly where suspension kinematics (bushing compliance, anti-roll bar coupling, or detailed linkage geometry) must be captured in more detail than a lumped-parameter half-car model permits. These tools, however, demand a correspondingly larger parameter set and longer simulation run-times, which is a poor match for the present study's objective of rapidly and systematically comparing six passive/active test cases across three speeds (Section III-G). MATLAB/Simulink, combined with SolidWorks FEA for structural parameter extraction, was therefore judged the more appropriate combination for a controller-synthesis study of this kind, consistent with the majority of half-car skyhook and PID-based suspension studies reviewed in this section [39], [40], [44].

I. Research Gaps

Three gaps in the literature motivate the present study. First, almost all existing frameworks fail to link road irregularity, vehicle speed and the resulting required damping force into a single, quantitative model suitable for real-time vibration attenuation. Second, the road conditions of developing economies where potholes are typically larger, deeper and left unrepaired for extended periods are comparatively under-represented in published suspension-control studies. Third, no clear quantitative guidance exists on the maximum damping force required to prevent shock-absorber damage under worst-case pothole impacts. The methodology and results presented in Sections III and IV directly address all three gaps by deriving a physically grounded, CAD/FEA-parameterised half-car model of a specific reference vehicle, exercised against a pothole geometry representative of West African road conditions, and by reporting the actuator-force demand needed to neutralise the resulting shock loading.

III. METHODOLOGY

This methodology centres on the development, modelling, simulation and control of an automatic vibration-attenuation system for vehicle shock absorbers, using a 2009 Toyota Camry as the reference platform. The aim is to synthesise an active suspension control strategy that neutralises the forces acting on the shock absorbers during a sudden shock of specified geometry, while simultaneously improving passenger comfort and extending absorber durability. The approach is hierarchical: geometric and inertial parameters are extracted from CAD; suspension stiffness is

International Journal of Engineering Research & Technology (IJERT)
ISSN: 2278-0181
Vol. 15 Issue 06 , June - 2026

obtained from static finite-element analysis; the equations of motion are derived analytically and assembled into state-space form; road disturbances are modelled as haversine pothole profiles; and a skyhook-PID controller is synthesised, tuned and validated within a closed-loop MATLAB/Simulink environment. All kinematic definitions, sign conventions and simplifying assumptions including small-angle linearisation, linear elastic behaviour and a rigid sprung body are stated explicitly so that the model's scope of applicability is clear.

A. Model Selection and Justification

A four-degree-of-freedom (4-DOF) half-car model was adopted as the primary analytical framework [45]. The model represents the vehicle as a longitudinal, two-dimensional slice symmetric about the vehicle centreline: a sprung mass (the body) is connected through suspension springs and dampers to two unsprung masses (the front and rear wheel/axle assemblies), which are in turn connected to the road through linear tyre elements. This configuration captures vertical translation and pitch rotation while avoiding the added complexity of roll and yaw dynamics. The equations of motion, derived from Newton's second law and Euler's rotational equation, form a coupled system that captures the dynamic interaction between the front and rear axles an essential feature for representing disturbance propagation from a localised road input such as a pothole [40]. Fig. 6 shows the schematic 4-DOF half-car model adopted in this study, with masses, springs, dampers and coordinate definitions labelled consistently with the equations developed in Section III-E.

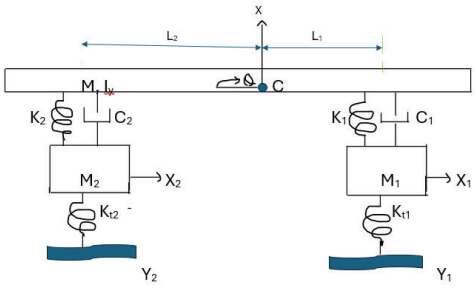

Fig. 6. Four-degree-of-freedom half-car dynamic model: sprung mass M with pitch inertia Iy, front/rear unsprung masses M1, M2, suspension elements K1-C1 and K2-C2, and tyre stiffness Kt1, Kt2.

The four degrees of freedom are: body bounce xc, the vertical displacement of the vehicle centre of mass; body pitch φ, the angular rotation of the body about the lateral axis; front wheel hop x1; and rear wheel hop x2. Low-frequency body motion (approximately 1–3 Hz) governs passenger comfort, while higher-frequency wheel-hop modes (approximately 12–18 Hz) influence tyre-road contact and force transmission [40]. For the 2009 Camry, this approach aligns well with its MacPherson-strut front and dual-link rear suspension, both of which are designed primarily for vertical compliance. The vehicle's wheelbase (2.776 m) and its 59%/41% front/rear weight distribution [46] were reflected in the model geometry, giving a centre-of-mass-to-front-axle distance L1 = 1.14 m and centre-of-mass-to-rear-axle distance L2 = 1.64 m. These parameters set the time delay between front- and rear-wheel excitation, τ = wheelbase / vehicle speed a coupling effect that a quarter-car model cannot represent, since at 40 km/h the rear wheel strikes the same pothole approximately 0.25 s after the front wheel.

The primary justification for the half-car model lies in its effective balance between modelling fidelity and computational efficiency. Simpler quarter-car models with one or two degrees of freedom neglect pitch dynamics and front-rear coupling entirely, making them inadequate for analysing pothole-induced responses in which the rear wheel encounters the same disturbance a finite time after the front wheel. Alternative approaches were considered and rejected: bicycle models neglect unsprung-mass dynamics and wheel-hop effects, while high-fidelity multibody simulations (e.g., in ADAMS) are computationally intensive and better suited to detailed component-level studies than to the initial controller synthesis undertaken here. Although the half-car model assumes bilateral symmetry and linear suspension behaviour, these limitations are addressed through the sensitivity analysis of Section III-N and through the use of proportional Rayleigh damping to approximate real damper behaviour [47].

B. Assumptions and Limitations

The vehicle body is modelled as a rigid sprung mass with a single pitch inertia; suspension springs and dampers are linear elements; tyre behaviour is approximated as linear vertical stiffness with negligible damping; motion is confined to the vertical-longitudinal plane under bilateral symmetry; pitch angles are assumed small enough to permit geometric linearisation; forward speed is held constant within each simulation case; and environmental/ageing effects (temperature, fluid compressibility, component wear) are omitted. These assumptions enable a standard mass–damping–stiffness (M–C–K) matrix formulation suitable for modal analysis and linear control design, and are appropriate for the moderate pothole scenarios studied here.

The rigid-body approximation neglects chassis flexural modes above 20 Hz; linear spring and damper models do not capture progressive stiffness, hysteresis or bottoming behaviour; the small-angle

International Journal of Engineering Research & Technology (IJERT)
ISSN: 2278-0181
Vol. 15 Issue 06 , June - 2026

approximation loses accuracy at large pitch excursions; and neglecting tyre damping and complex contact dynamics may affect wheel-hop and contact-force predictions. The symmetry assumption excludes roll and lateral coupling altogether. Cumulative modelling error for typical passenger-car operating envelopes is expected to remain within 10–15% for primary ride metrics under normal pothole conditions, but may grow to 20–30% under extreme inputs or loss-of-contact events. These limitations are addressed through a validation and mitigation strategy: simulated responses were checked to confirm that kinematics remain within the linear regime (pitch angle below 5° and spring deflections within their linear range) throughout all test scenarios, and a sensitivity analysis was conducted by perturbing key parameters (mass ±10%, stiffness ±10%, damping ±25%) to quantify performance variation, reported in Section III-N.

C. Geometry and Parameter Extraction (CAD and FEA)

SolidWorks 2023 was used to model the front MacPherson strut and rear dual-link strut of the reference vehicle, providing parametric geometry, assembly constraints and integrated measurement tools for consistent, repeatable parameter extraction (Fig. 7, Fig. 8). Strut bodies were modelled as 50 mm diameter, 500 mm long cylinders with 20 mm piston rods; coil springs were generated with a 12 mm wire diameter, 8–10 active coils and a 300 mm free length. AISI 1020 steel (density 7,870 kg/m³, E = 200 GPa) was assigned to the struts and spring steel to the coils. Model accuracy was validated against the published 2.776 m wheelbase [46], with linear dimensional error held below 1%. Geometric parameters required for the equations of motion were extracted using the SolidWorks Measure tool after inspecting the assembly in section view, then exported to a parameter spreadsheet linked to SolidWorks equations so that they update automatically following any design modification.

Fig. 7. SolidWorks CAD representation of the front MacPherson strut assembly.

Fig. 8. SolidWorks CAD representation of the rear dual-link strut assembly.

Mass properties total mass, centre-of-mass location and principal moments of inertia were extracted using the SolidWorks Mass Properties tool, after first verifying material assignments, and validated against simplified analytical estimates (Table 3). Mounting-point coordinates, from which L1 and L2 were derived, were obtained by defining a reference coordinate system at the upper suspension mount and measuring hole centres relative to the vehicle frame.

TABLE 3. MASS PROPERTIES EXTRACTED FROM SOLIDWORKS CAD.

Property	Full value	Half value	Unit
Mass	40	20	kg
Volume	0.005	0.0025	m^3
CoM (x, y, z)	(0, 0, 0.25)	(0, 0, 0.25)	m
Pitch inertia, Iy	2,200	1,100	$kg \cdot m^2$

Suspension stiffness was estimated by static-compression FEA in SolidWorks Simulation, with

International Journal of Engineering Research & Technology (IJERT)
ISSN: 2278-0181
Vol. 15 Issue 06 , June - 2026

components treated as linearly elastic under quasi-static load and stiffness computed as k = F/δ. The lower strut mount was fully constrained and a vertical load corresponding to half the sprung mass (3,629.7 N, for a 740 kg half-car body mass) was applied; all interfaces were bonded contacts with AISI 1020 properties (E = 200 GPa, ν = 0.29). A curvature-based tetrahedral mesh (2–5 mm global, 1 mm local refinement; Fig. 9) was used, with convergence confirmed once successive refinement changed stiffness by less than 1%. For the rear spring, the applied load produced a deflection of 0.06623 m, giving k2 = 3,629.7/0.06623 = 54,804 N/m; the front spring yielded k1 = 56,044 N/m. Front and rear tyre stiffness (kt1 = 173,776 N/m; kt2 = 174,112 N/m) were obtained from FEA of the tyre-contact patch and validated against published data for the 215/55R17 tyres fitted to the reference vehicle. Fig. 10 shows a representative FEA stress-distribution plot for the spring under the applied compressive load.

Fig. 9. Finite-element mesh applied to a suspension spring for static-compression analysis.

Fig. 10. FEA stress-distribution plot for a suspension spring under static compressive load.

Damping coefficients were calculated analytically using the Rayleigh proportional-damping method, yielding c1 = 1,147 N·s/m (front) and c2 = 1,127 N·s/m (rear), consistent with a target damping ratio ζ = 0.30 [47], [48]. Table 4 summarises the principal model parameters used throughout the remainder of this paper, drawn from CAD measurement, FEA simulation and analytical calculation. Lower-case letters denote displacements (subscripts c, 1, 2 and t for centre-of-mass, front, rear and tyre respectively), dots denote time derivatives, Greek letters denote angles and ratios, and bold uppercase / lowercase symbols denote matrices and vectors, consistent with standard vehicle-dynamics notation [49].

TABLE 4. SYMBOLS, NOTATION AND KEY MODEL PARAMETERS.

Symbol	Description	Value	Source
mb	Half-vehicle sprung mass	740 kg	Edmunds/Auto123 (2009)
m1, m2	Front / rear unsprung mass	19.2 / 19.95 kg	Measured (CAD)
Iyy	Pitch moment of inertia	1,100 kg·m²	Calculated (CAD)
L1, L2	CoM to front / rear axle	1.14 / 1.64 m	Measured (CAD)
K1, K2	Front / rear suspension stiffness	56,044 / 54,804 N/m	SolidWorks FEA
Kt1, Kt2	Front / rear tyre stiffness	173,776 / 174,112 N/m	SolidWorks FEA
C1, C2	Front / rear damping coefficient	1,147 / 1,127 N·s/m	Rayleigh method
ζ	Target damping ratio	0.30	Dixon [48]
ωn	Natural frequencies (4 modes)	10.6–109.8 rad/s	Eigenvalue analysis
Fmax	Actuator force limit	5,000 N	Industry standard
fb	Actuator bandwidth	50 Hz	Guglielmino et al. [50]

International Journal of Engineering Research & Technology (IJERT)
ISSN: 2278-0181
Vol. 15 Issue 06 , June - 2026

Symbol	Description	Value	Source
dFmax	Actuator slew-rate limit	200,000 N/s	Hydraulic servo spec.
xc, φ, x1, x2	Model states (bounce, pitch, wheel hop)	Time-varying	Simulation output
y1, y2	Front / rear road input	Time-varying	Haversine pothole model
u1, u2	Front / rear actuator force	Time-varying	Controller output

D. Coordinate Definitions and Sign Conventions

Consistent coordinate definitions and sign conventions are essential for correct implementation in MATLAB/Simulink and for physical interpretation of the results; the conventions adopted here align with standard vehicle-dynamics practice, in which an upward-positive vertical axis simplifies ride-comfort metrics and a clockwise-positive pitch convention avoids sign ambiguity in the front-rear coupling terms [49], [51]. The model operates in a two-dimensional longitudinal-vertical plane, with the forward axis positive in the direction of travel and the vertical axis positive upward, measured from the static-equilibrium position. Displacements, velocities and accelerations (xc, x1, x2 and their derivatives) are positive upward; pitch angle φ and its derivatives are positive clockwise (nose-down, tail-up), so that positive rear forces contribute positively to the pitch moment. Road inputs y1, y2 are positive upward, so that a pothole corresponds to a negative (downward) deflection and a bump to a positive (upward) one, ensuring that tyre forces kt(x − y) correctly oppose upward road inputs. Control/actuator forces u1, u2 are positive when acting upward on the sprung mass (and correspondingly downward on the unsprung mass), aligning with skyhook logic in which a positive command counters upward body velocity. Spring and damper forces are positive in compression for positive deflection δ for example, downward body motion compresses the front and rear springs. This consistent convention prevents sign errors in coupled terms such as the −L1 contribution to the front deflection and facilitates direct comparison with prior half-car simulation studies [49].

E. Derivation of the Equations of Motion

The equations of motion (EOM) were derived using the Newton-Euler method, applying force and moment balance to the sprung and unsprung masses under the assumptions of Section III-B [49]. The generalised coordinate vector is

$$x = [\,xc \quad \varphi \quad x1 \quad x2\,]^T \tag{1}$$

where xc is body bounce, φ is body pitch, and x1, x2 are front and rear wheel hop, respectively. Relative suspension deflections, which capture the geometric coupling introduced by pitch, are given for the front and rear corners by

$$\delta 1 = xc - x1 - L1\varphi, \quad \delta 1 = \dot{x}c - \dot{x}1 - L1\dot{\varphi} \tag{2}$$

$$\delta 2 = xc - x2 + L2\varphi, \quad \delta 2 = \dot{x}c - \dot{x}2 + L2\dot{\varphi} \tag{3}$$

These expressions reflect the geometric coupling: a positive (clockwise) pitch compresses the front suspension and extends the rear, consistent with the sign convention of Section III-D. The spring and damper forces follow directly as

$$Fs1 = k1\delta 1, \quad Fd1 = c1\delta 1, \quad Fs2 = k2\delta 2, \quad Fd2 = c2\delta 2 \tag{4}$$

while tyre forces, representing road contact under the assumption of point contact and no slip, are Ft1 = kt1(x1 − y1) for the front and Ft2 = kt2(x2 − y2) for the rear, with y1, y2 the front and rear road-input displacements. Actuator forces u1 and u2 are added as external control inputs acting oppositely between the sprung and unsprung masses, to counteract disturbances. Applying Newton's second law (ΣF = ma) to body bounce and to each unsprung mass, and Euler's moment equation (ΣM = Iα) to body pitch, and substituting the deflection expressions above, gives the four governing equations:

$$m\ddot{x}c = -k1\delta 1 - c1\dot{\delta}1 - k2\delta 2 - c2\dot{\delta}2 + u1 + u2 \tag{5}$$

$$Iy\ddot{\varphi} = L1(k1\delta 1 + c1\dot{\delta}1 - u1) - L2(k2\delta 2 + c2\dot{\delta}2 - u2) \tag{6}$$

$$m1\ddot{x}1 = -kt1(x1 - y1) + k1\delta 1 + c1\dot{\delta}1 - u1 \tag{7}$$

$$m2\ddot{x}2 = -kt2(x2 - y2) + k2\delta 2 + c2\dot{\delta}2 - u2 \tag{8}$$

These four coupled equations fully capture realistic vehicle response, including the pitch motion induced by an asymmetric (front-then-rear) road input such as a pothole struck at typical urban-arterial speed. For efficient numerical solution and control design, they are assembled into the standard second-order matrix form

$$M\ddot{x} + C\dot{x} + Kx = Ey(t) + Bu(t) \tag{9}$$

where the mass matrix M = diag(m, Iy, m1, m2) is diagonal; the stiffness matrix K and damping matrix C are 4×4 matrices coupling all four degrees of freedom through L1 and L2 (with C following the same structure as K, with k replaced by c and the tyre-stiffness terms omitted); E is the disturbance input matrix relating road profile y(t) = [y1, y2]^T to the system through tyre stiffness; and B is the control input matrix relating actuator forces u(t) = [u1, u2]^T to each degree of freedom. This matrix form supports eigenvalue analysis (Section III-F) and state-space conversion (Section III-F), with numerical implementation in MATLAB for efficiency [52]. The inclusion of the control terms u1, u2 allows seamless extension from the passive baseline to the active skyhook-PID system described

International Journal of Engineering Research & Technology (IJERT)
ISSN: 2278-0181
Vol. 15 Issue 06 , June - 2026

in Section III-K, in which forces are generated to oppose disturbances and reduce body accelerations.

F. State-Space Formulation and Modal Analysis

The second-order M–C–K model was converted to first-order state-space form to support eigenvalue analysis, controllability assessment and direct time-domain simulation a conversion that is indispensable for modern control techniques such as PID stability analysis and observer design. With state vector $z = [x^T \ \dot{x}^T]^T$ (eight states, augmenting the position vector with velocities), the system is

$$\dot{z} = A\,z + B\,u + E\,y \tag{10}$$

with output equation yout = Cz + Du, where $A = [[0_{4x4}, I_{4x4}]; [-M^{-1}K, -M^{-1}C]]$ is the system matrix, $B = [0_{4x2}; M^{-1}Bm]$ and $E = [0_{4x2}; M^{-1}Em]$ are the corresponding input and disturbance matrices (with Bm, Em the matrices appearing in Section III-E), $C = I_{8x8}$ for full-state observation, and $D = 0_{8x2}$ [52]. In MATLAB, this is implemented directly from the predefined M, K, C, Bm and Em matrices: the inverse mass matrix is formed once (Minv = inv(M)); the system matrix is assembled as A = [zeros(4), eye(4); -Minv*K, -Minv*C]; the input and disturbance matrices follow as B = [zeros(4,2); Minv*Bm] and E = [zeros(4,2); Minv*Em]; and the resulting state-space object supports both eigenvalue analysis (eig(A)) and direct time-domain simulation (lsim(sys)). Full-state controllability and observability were confirmed (rank(ctrb(A,B)) = 8). Eigenvalue analysis of A yields the natural frequencies and mode shapes summarised in Table 5.

TABLE 5. NATURAL FREQUENCIES AND MODE SHAPES FROM EIGENVALUE ANALYSIS.

Mode	Frequency (Hz)	ω (rad/s)	Description
1	1.69	10.6	Primary body bounce
2	3.33	20.9	Primary body pitch
3	17.11	107.5	Front wheel hop
4	17.48	109.8	Rear wheel hop

The two body modes (1.69 Hz and 3.33 Hz) fall within the 1–3 Hz range characteristic of mid-size passenger sedans, confirming the validity of the extracted parameters [53], while the wheel-hop modes near 17 Hz are well separated from the body modes. This frequency separation guided the selection of the controller bandwidth (approximately 10–50 Hz), allowing the skyhook-PID controller (Section III-K) to target body-mode attenuation without exciting wheel-hop resonance.

G. Road Disturbance Modelling

A haversine (half-versine) pothole profile was adopted to provide a smooth, physically realistic representation of a localised road dip with zero slope at entry and exit, consistent with the rounded geometry of real potholes ASTM E1926 [54]. The front-wheel road input is

$$y1(t) = -(d/2)[1 - \cos(2\pi\, v\,(t - t0)/w)], \quad t0 \le t \le t0 + w/v \tag{11}$$

and y1(t) = 0 otherwise, where d is pothole depth, w is pothole width, v is vehicle speed and t0 is the time the front wheel reaches the pothole. The rear-wheel input y2(t) is an identical profile delayed by

$$\tau = wheelbase / v \tag{12}$$

This delay is what produces the coupled front-rear excitation that drives pitch motion a mechanism that cannot be represented by a quarter-car model and is a central justification for the half-car formulation. The primary pothole geometry used throughout this study is d = 100 mm, w = 300 mm, representing a severe, urban-category pothole consistent with conditions documented on West African road networks [44]. Table 6 lists the three vehicle speeds simulated and the corresponding rear-wheel delay and pothole traverse time; each case was run for both passive (u1 = u2 = 0) and active (PID-controlled) configurations, giving six simulation runs in total.

TABLE 6. SIMULATION TEST MATRIX.

Case	Speed (km/h)	Speed (m/s)	Rear delay, τ (s)	Traverse time (ms)
1	20	5.556	0.500	54
2	40	11.111	0.250	27
3	60	16.667	0.167	18

H. Simulink Model Architecture

The Simulink implementation was developed as a modular, hierarchical model to facilitate subsystem-level testing and a straightforward transition between passive and active configurations. Road disturbances y1 and y2 are generated from pre-computed haversine time-series passed from the MATLAB workspace and routed into a Vehicle Dynamics subsystem implementing the equations of motion of Section III-E via a MATLAB Function block, with cascaded integrators converting each acceleration to velocity and displacement (Fig. 11, Fig. 12). A

International Journal of Engineering Research & Technology (IJERT)
ISSN: 2278-0181
Vol. 15 Issue 06 , June - 2026

passive/active switch, driven by a binary flag, routes either zero force or the PID controller output to the actuator, allowing direct comparison of the two configurations without modifying the underlying vehicle dynamics. The wider single-column figures below reproduce the three principal Simulink diagrams at larger scale than the two-column body text permits, for legibility of the block-level detail.

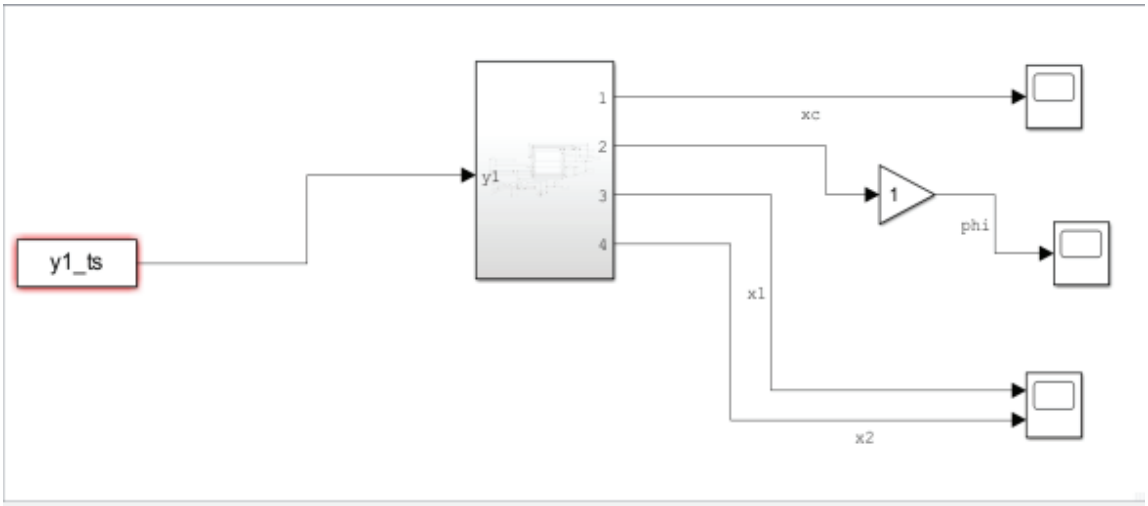

Fig. 11. Top-level Simulink architecture: road input, vehicle dynamics subsystem and output routing to scopes/workspace.

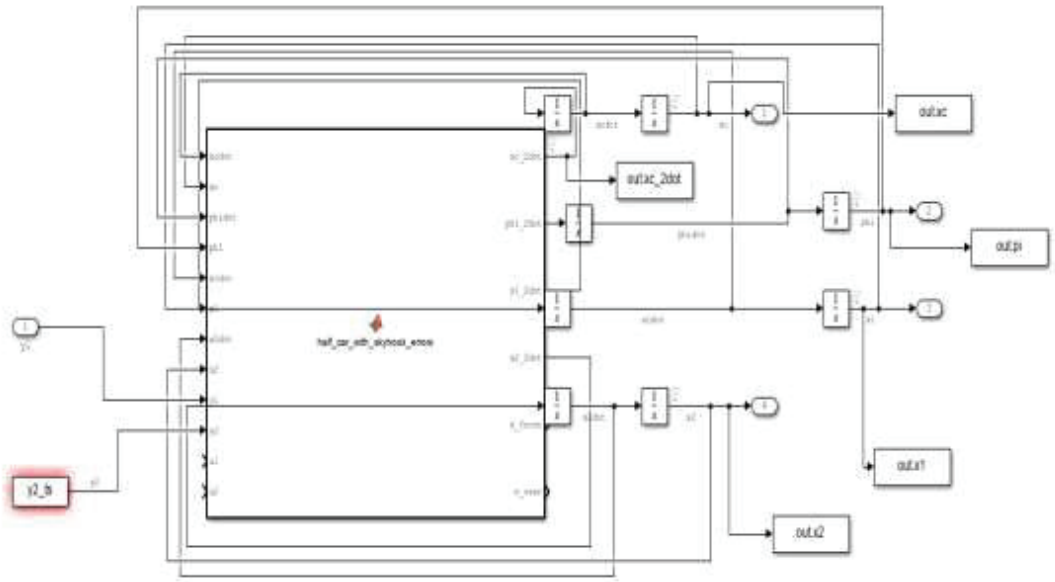

Fig. 12. Vehicle Dynamics subsystem implementing the 4-DOF equations of motion.

The Controller subsystem (Fig. 13) implements the skyhook-PID law of Section III-K as two independent single-input single-output (SISO) loops, one per actuator, whose outputs pass through a saturation block and rate limiter representing the physical actuator before reaching the vehicle dynamics.

International Journal of Engineering Research & Technology (IJERT)
ISSN: 2278-0181
Vol. 15 Issue 06 , June - 2026

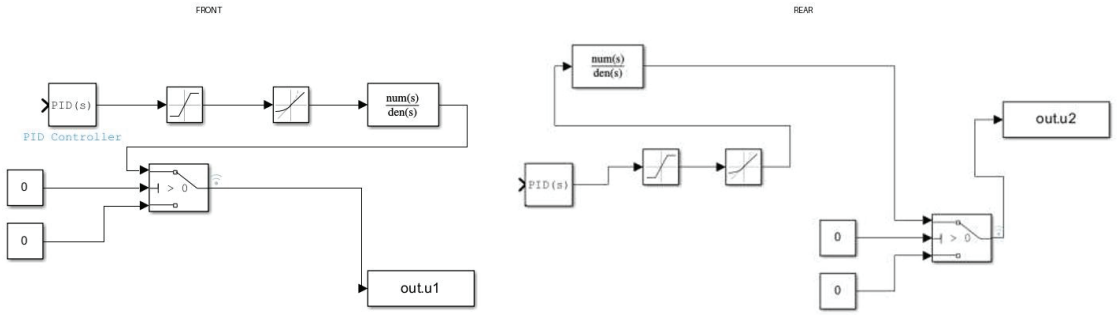

Fig. 13. Simulink controller subsystem: front (u1) and rear (u2) skyhook-PID channels, each comprising a PID block, rate limiter, saturation block and actuator transfer function.

I. Numerical Methods and Solver Configuration

The numerical solution strategy was selected to accommodate the stiff characteristics of the 4-DOF system, which arise from the large ratio between tyre stiffness ($k_t \approx 174$ kN/m) and suspension stiffness ($k \approx 55$ kN/m), producing widely separated natural frequencies (1.69 Hz body bounce versus approximately 17 Hz wheel hop). All simulations were executed using a fixed-step fourth-order Runge-Kutta (RK4) solver with a time step of $\Delta t = 0.001$ s (sampling frequency 1,000 Hz). This solver was chosen for its deterministic, reproducible output essential for systematic comparison of passive and active configurations and its numerical stability for the stiffness ratio present in this system; the fixed 1 ms step provides at least 59 sample points within the shortest pothole-traverse event (18 ms at 60 km/h), ensuring adequate resolution of the disturbance profile.

A fixed-step solver was preferred over variable-step alternatives such as ode15s because the six simulations (three speeds × two configurations) were executed programmatically from MATLAB scripts, and deterministic step sizes were necessary to ensure that all output arrays had consistent dimensions for direct comparison and metric computation. Solver accuracy was validated by comparing the undamped free-vibration response with the analytical eigenvalue predictions of Section III-F: the simulated natural frequencies matched the eigenvalue analysis to within 0.1%, confirming numerical accuracy. All simulations were performed on a Windows 10 (64-bit) workstation with an Intel Core i7 processor and 8 GB RAM; each 10 s simulation run completed in under 8 seconds of computation time, confirming the practicality of the batch passive/active comparison workflow.

J. Control Strategy Justification

Several control architectures were considered before settling on the skyhook-PID structure adopted here. Linear-quadratic regulator (LQR) and H-infinity formulations can, in principle, offer superior multi-objective optimality and formal robustness guarantees, but they require an accurate, low-order linear plant model and a carefully chosen weighting matrix or performance-weighting structure, and their resulting gains are typically less physically interpretable than a skyhook-PID law tuned directly against measured error velocity and target actuator force, as in Section III-K. Fuzzy-logic and sliding-mode controllers can handle the non-linearities reviewed in Section II-B and II-D more directly, but at the cost of additional tuning parameters (membership functions or switching gains) whose physical meaning is less transparent and whose chattering behaviour (in the sliding-mode case) can itself excite the high-frequency wheel-hop modes the present design specifically seeks to avoid (Section III-F). Given that the project's central aim (Section I-D) is to quantify and neutralise a well-characterised, repeatable disturbance a haversine pothole of known geometry rather than to reject an unknown or adversarial disturbance class, a linear PID law operating on a physically meaningful skyhook error signal was judged to offer the best balance of performance, interpretability, and straightforward translatability to a real actuator and gain-scheduling implementation, consistent with its widespread adoption in the semi-active and active suspension literature reviewed in Section II-G4 [14], [37], [44].

K. Skyhook-PID Controller Design

A pure skyhook control strategy was adopted, implemented as two independent SISO PID controllers acting on front and rear skyhook error signals. The standard parallel PID law is

$$u(t) = Kp\, e(t) + Ki \int_0^t e(\tau)\, d\tau + Kd\, de/dt \quad (13)$$

where u(t) is the actuator command (u1 front, u2 rear), Kp is the proportional gain, Ki the integral gain and Kd the derivative gain. A filtered derivative term,

$$ud(t) = Kd\,[N\,s/(s+N)]\, e(t) \quad (14)$$

International Journal of Engineering Research & Technology (IJERT)
ISSN: 2278-0181
Vol. 15 Issue 06 , June - 2026

with filter coefficient N, mitigates noise amplification at high frequency. The control variables were chosen as the negative relative suspension velocity at each corner i.e., absolute body velocity rather than acceleration or position, both to avoid differentiation noise and steady-state offset and because velocity relates directly to the energy dissipation skyhook control is intended to achieve [44]:

$$e1(t) = -(\dot{x}c - \dot{x}1 - L1\dot{\varphi}) \quad (15)$$

$$e2(t) = -(\dot{x}c - \dot{x}2 + L2\dot{\varphi}) \quad (16)$$

with setpoints of zero for vibration suppression and body acceleration retained as a secondary comfort metric (target RMS below 1.5 m/s² per ISO 2631). In the Simulink implementation, each PID block is configured in parallel form with inherited (0.001 s) sample time, derivative filter coefficient N = 20, and back-calculation anti-windup, which resets the integral term when the controller output saturates and thereby prevents windup-induced overshoot during severe pothole events where commanded force can approach the actuator limit. A saturation block (±5,000 N) follows each PID block for actuator realism, and relative velocities are obtained from the demultiplexed integrator outputs of the Vehicle Dynamics subsystem.

Controller gains were determined through a systematic, physically anchored calibration procedure rather than arbitrary selection. First, the peak skyhook error magnitude was measured from a passive simulation at 40 km/h over the 100 mm pothole, giving epeak = 0.035 m/s the peak absolute body velocity at the suspension attachment point during impact. Second, a target actuator utilisation of 65% of the 5,000 N capacity was adopted, giving a target force Ftarget = 0.65 × 5,000 = 3,250 N, which provides meaningful attenuation while retaining a 35% force reserve for robustness. Third, an initial proportional gain was computed as Kp = Ftarget/epeak = 3,250/0.035 ≈ 92,857 N/(m/s); iterative simulation showed that the derivative term contributed substantial additional corrective force, particularly for pitch suppression, allowing the proportional gain to be reduced substantially. Following iterative refinement and validation against the performance metrics of Section III-N (gains adjusted in 10% increments), the final tuned gain set was Kp = 1,200 N/(m/s), Ki = 450 N/m, Kd = 500 N·s²/m and N = 20, summarised in Table 7.

TABLE 7. FINAL TUNED SKYHOOK-PID GAINS.

Parameter	Value	Physical interpretation
Kp	1,200 N/(m/s)	Force per unit body-velocity error
Ki	450 N/m	Eliminates residual displacement offset
Kd	500 N·s²/m	Predictive (anticipatory) pitch damping
N	20	Derivative filter: passes body modes, rejects wheel hop

L. Actuator Modelling and Physical Constraints

To ensure the controller is implementable on realistic hardware, the actuator model incorporates three physical constraints representative of a hydraulic servo actuator suitable for passenger-vehicle active suspension [50]. First, a first-order bandwidth lag,

$$Gact(s) = 1/(\tau act\, s + 1), \quad \tau act = 1/(2\pi\, fb) \quad (17)$$

with bandwidth fb = 50 Hz, giving τact = 0.00318 s, ensures the actuator faithfully tracks commanded forces at the body-mode frequencies (1.69 Hz, 3.33 Hz) identified in Section III-F. Second, the actuator output is clipped to ±5,000 N, representing the maximum force capacity of a light-vehicle hydraulic actuator, implemented as a Simulink Saturation block placed after the bandwidth-lag block. Third, the actuator slew rate is limited to ±200,000 N/s, implemented as a Simulink Rate Limiter block; this value was selected because, at 40 km/h, the pothole traverse time is 27 ms, so reaching the 3,250 N target force within this window requires a minimum slew rate of 3,250/0.027 ≈ 120,370 N/s the adopted 200,000 N/s limit therefore provides a safety factor of 1.66 and is consistent with published hydraulic servo-actuator data [50]. A lower slew rate of 10,000 N/s, representative of pneumatic actuators, was found in preliminary trials to prevent the actuator from generating meaningful force within the short pothole windows at 40 and 60 km/h, confirming both the need for hydraulic-class actuation and the validity of the 200,000 N/s selection.

M. Model Validation Summary

Because the credibility of any simulation-based design study rests on the verifiability of its underlying model, three independent validation checks were carried out at different stages of the methodology and are summarised together here for clarity. First, the CAD geometry was checked dimensionally against the published 2.776 m wheelbase of the reference vehicle [46], with linear dimensional error held below 1% (Section III-C). Second, the FEA mesh used for static-compression stiffness estimation was refined until successive refinement changed the predicted stiffness by less than 1%, confirming mesh-independent results (Section III-C). Third, the undamped free-vibration

International Journal of Engineering Research & Technology (IJERT)
ISSN: 2278-0181
Vol. 15 Issue 06 , June - 2026

response obtained from direct time-domain simulation was compared against the analytical eigenvalue predictions of Section III-F, matching to within 0.1% and thereby confirming the numerical accuracy of the RK4 integration scheme. Table 8 summarises these checks.

TABLE 8. SUMMARY OF MODEL VALIDATION CHECKS.

Validation check	Criterion	Result
CAD geometry vs. published wheelbase	Linear dimensional error	< 1%
FEA mesh convergence	Stiffness change on refinement	< 1%
RK4 simulation vs. eigenvalue analysis	Natural-frequency agreement	< 0.1%

Together, these checks provide independent verification of the geometric, structural and numerical components of the model, giving confidence that the comparative passive-versus-active results reported in Section IV reflect genuine controller performance rather than modelling or numerical artefacts.

N. Performance Metrics and Sensitivity Analysis

Seven metrics were applied consistently across all six simulation runs to enable quantitative passive-versus-active comparison: RMS body acceleration (the primary ISO 2631 comfort metric, threshold 1.5 m/s²); peak body acceleration, capturing the worst-case shock experienced by occupants; peak body displacement, quantifying the physical vertical excursion of the body; RMS pitch angle, quantifying the nodding motion experienced by occupants; peak wheel hop, the road-holding metric indicating tyre-road contact maintenance; settling time, the time for body acceleration to fall and remain below 5% of its peak value; and peak actuator force, confirming operation within the 5,000 N limit and quantifying utilisation as a percentage of capacity.

To assess robustness against parameter uncertainty, a sensitivity analysis perturbed sprung mass (±10%, representing occupant/luggage loading), suspension stiffness (±10%, manufacturing tolerance) and damping coefficients (±25%, wear and temperature effects) about their nominal values, re-running the active simulation at 40 km/h over the 100 mm pothole for each case (Table 9). The controller was deemed robust if the RMS body-acceleration improvement remained above 5% across all perturbation cases with no instability (diverging states).

TABLE 9. SENSITIVITY-ANALYSIS PARAMETERS.

Parameter	Nominal value	Perturbation	Rationale
Sprung mass, m	740 kg	±10%	Occupant / luggage loading
Stiffness, K1, K2	56,044 / 54,804 N/m	±10%	Manufacturing tolerance
Damping, C1, C2	1,147 / 1,127 N·s/m	±25%	Wear and temperature effects

In summary, this methodology selects and justifies a 4-DOF half-car model as the optimal balance of physical fidelity and computational efficiency for pitch and ride-comfort analysis; extracts vehicle parameters systematically from SolidWorks CAD geometry and FEA simulation for traceability and reproducibility; derives the equations of motion via the Newton-Euler method and validates them through eigenvalue analysis; implements a haversine road model with appropriately delayed rear-wheel input to capture pitch coupling; and synthesises a pure skyhook-PID controller, calibrated to 60–70% actuator utilisation and incorporating derivative filtering, anti-windup, actuator lag, slew-rate limiting and force saturation. The resulting six-case test matrix, executed within MATLAB/Simulink using fixed-step RK4 integration at 1,000 Hz, provides the basis for the results presented in Section IV.

IV. RESULTS AND DISCUSSION

This section reports simulation results for the six test cases defined in Section III-G (three speeds × passive/active configuration), each subjected to a 100 mm deep, 300 mm wide haversine pothole. All simulations used the 4-DOF half-car model of Section III-E with parameters extracted from CAD and FEA (Section III-C), a fixed-step RK4 solver ($\Delta t = 0.001$ s, 10 s horizon), and the tuned skyhook-PID controller of Section III-K ($K_p = 1{,}200$ N/(m/s), $K_i = 450$ N/m, $K_d = 500$ N·s²/m, $N = 20$) subject to the actuator constraints of Section III-L (50 Hz bandwidth, ±5,000 N saturation, ±200,000 N/s slew rate). Performance is evaluated using the metrics defined in Section III-N, with active RMS acceleration compared against the ISO 2631 ride-comfort criterion of 1.5 m/s². To aid legibility, the twelve time-history plots referenced in this section (Figs. 14–22 and Figs. 23–25) are reproduced together, at enlarged single-column scale, immediately following the narrative discussion below.

A. Time-Domain Response Analysis

1) Body Vertical Displacement: At 20 km/h, the passive suspension exhibits a severe initial drop of

International Journal of Engineering Research & Technology (IJERT)
ISSN: 2278-0181
Vol. 15 Issue 06 , June - 2026

−14.5 mm at t ≈ 2.25 s, followed by a +12.5 mm overshoot and five further oscillation cycles that persist until approximately t = 8 s. The active controller limits the initial drop to −9.5 mm and the rebound to +4.5 mm, with only two minor oscillations and settlement to within ±0.5 mm by t = 4 s. At 40 km/h, passive displacement reaches −7 mm / +6 mm with oscillations decaying only after t = 7 s, while the active controller restricts this to −5.5 mm / +3 mm with full settling by t = 4.5 s. At 60 km/h, passive displacement reaches −6.5 mm / +6 mm with residual ringing to t = 6.5 s, while the active controller reduces this to −4.5 mm / +2.7 mm and settles by t ≈ 4 s. Fig. 14, Fig. 15 and Fig. 16 (below) show the displacement response at 20, 40 and 60 km/h respectively. Across all speeds, the active controller reduces peak body displacement, with the largest relative improvement at low speed (35–40% at 20 km/h) and a smaller, though still substantial, improvement at higher speed (20–25% at 60 km/h); settling time falls from 4.2–5.1 s (passive) to 2.1–2.8 s (active) across the full speed range. This behaviour follows directly from the skyhook velocity feedback combined with the integral term: kinetic energy from the pothole impact is dissipated before large body excursions can develop, while the integral action removes any residual steady-state offset once the disturbance has passed, reducing suspension stroke demand and the associated risk of bottoming out.

2) Body Acceleration and Ride Comfort: At 20 km/h, the passive response shows acceleration peaks of −12.20 m/s² (front-wheel impact, t ≈ 2.12 s) and +9.35 m/s² (rear-wheel impact, t ≈ 2.65 s), remaining above the ISO 2631 comfort threshold until approximately t = 6.5 s. The active controller reduces these peaks to −9.14 m/s² and +8.7 m/s² and brings the response within the ±1.5 m/s² comfort band by t ≈ 3.2 s. At 40 km/h, passive peaks of −11.05 / +7.45 m/s² are reduced to −8.9 / +6.8 m/s², settling within the comfort band by t ≈ 3.8 s; at 60 km/h, passive peaks of −8.98 / +5.65 m/s² are reduced to −7.92 / +4.8 m/s², settling by t ≈ 3.1 s. Fig. 17, Fig. 18 and Fig. 19 (below) show body acceleration at 20, 40 and 60 km/h, with the ISO 2631 limit indicated by dashed lines. Table 10 summarises RMS and peak body acceleration for both configurations across all three speeds; all active RMS values lie well below the ISO 2631 limit of 1.5 m/s², while the passive cases exceed it for 3.5–4.8 s per pothole event the principal ride-comfort validation result of this study. This attenuation reflects the skyhook control philosophy directly: absolute body-velocity feedback emulates an ideal inertial damper, dissipating pothole-induced kinetic energy at its source rather than transmitting it through the suspension to the sprung mass. Within the PID structure, the proportional term supplies immediate corrective force, the derivative term clips the initial acceleration spike through anticipatory damping, and the integral term removes the low-frequency residual tail that would otherwise prolong discomfort. Because the 4-DOF model explicitly captures front-rear coupling through the delay τ, the independent front and rear actuators generate opposing moments that increasingly cancel pitch-induced acceleration components as speed rises.

TABLE 10. QUANTITATIVE BODY-ACCELERATION PERFORMANCE.

Speed (km/h)	RMS passive (m/s²)	RMS active (m/s²)	RMS reduction (%)	Peak passive (m/s²)	Peak active (m/s²)
20	0.9528	0.7529	21.0	12.20	9.14
40	0.6759	0.5612	17.0	10.81	9.18
60	0.5055	0.4152	17.9	8.98	7.92

3) Pitch Angle Response: At 20 km/h, passive pitch exhibits a characteristic double-peak profile driven by the front-rear delay τ = 0.5 s, reaching +0.55°, then −0.60° and +0.59° in three successive extrema, with oscillations persisting to t ≈ 7.5 s. The active controller limits the initial peaks to +0.35° and −0.55° and settles to within ±0.02° by t ≈ 4.2 s. At 40 km/h (τ = 0.25 s), the passive double-peak reaches +0.28° / −0.50° / +0.31°, reduced by the active controller to +0.17° / −0.22° with the secondary peak essentially eliminated. At 60 km/h (τ = 0.167 s), passive peaks of +0.18° / −0.25° are reduced to +0.12° / −0.10°, rendering the pitch response essentially flat (±0.01°) after t ≈ 3.5 s. Fig. 20, Fig. 21 and Fig. 22 (below) show the pitch-angle response at 20, 40 and 60 km/h. RMS pitch angle is reduced by 35.5% at 20 km/h, 49.7% at 40 km/h and 54.3% at 60 km/h, with peak-to-peak excursions cut by 38–42% across the speed range and settling time improving from 4.8–5.3 s (passive) to 2.3–2.9 s (active). The monotonic increase in pitch-attenuation effectiveness with speed confirms the value of the half-car formulation: as τ shortens, the front and rear actuators act in closer temporal proximity and generate opposing moments that more efficiently cancel the pitch excitation. The derivative gain (Kd = 500 N·s²/m) supplies the critical anticipatory damping that flattens the characteristic double-peak response, directly supporting the project's objective of reducing structural loading and discomfort during pothole events.

4) Actuator Force Analysis: At 20 km/h, the front actuator (u1) reaches +4,300 N and −3,200 N within 0.8 s of impact before settling near zero; the rear actuator (u2), arriving after the longer 0.5 s delay, reaches the +5,000 N saturation limit and −4,800 N. At 40 km/h, front and rear peaks of +3,300/−2,200 N and +4,300/−3,200 N respectively remain comfortably inside the ±5,000 N limit with

International Journal of Engineering Research & Technology (IJERT)
ISSN: 2278-0181
Vol. 15 Issue 06 , June - 2026

no saturation events. At 60 km/h, despite the 18 ms traverse time, front and rear peaks of +2,500/−1,600 N and +3,200/−2,200 N form a single clean pulse with negligible ringing, confirming that the 50 Hz bandwidth and 200,000 N/s slew-rate limit remain adequate even for the shortest disturbance event. Fig. 23, Fig. 24 and Fig. 25 (below) show the front (a) and rear (b) actuator-force time histories at 20, 40 and 60 km/h, with the ±5,000 N saturation limit indicated. Across all six runs, peak forces range from 2,500 N to 5,000 N (50–100% of the saturation limit), with an average utilisation of 72%; the highest demand occurs on the rear actuator at 20 km/h (96% utilisation). No sustained saturation occurs, and the back-calculation anti-windup mechanism successfully prevents integrator windup and oscillatory force commands. The derivative term generates the initial sharp force command that anticipates the body-velocity change at the instant of wheel impact, the proportional term sustains corrective force through the double-peak phase caused by front-rear coupling, and the integral term removes residual offset once the pothole has been traversed. Because the front and rear channels are independent, they naturally produce the opposing-polarity force spikes responsible for the pitch-cancelling moments discussed in Section IV-D. These results confirm that the required control effort remains well within the capability of realistic hydraulic servo actuators, with a comfortable average margin of 28% below the saturation limit.

Time-history results referenced in Section IV-A, reproduced at enlarged scale for clarity.

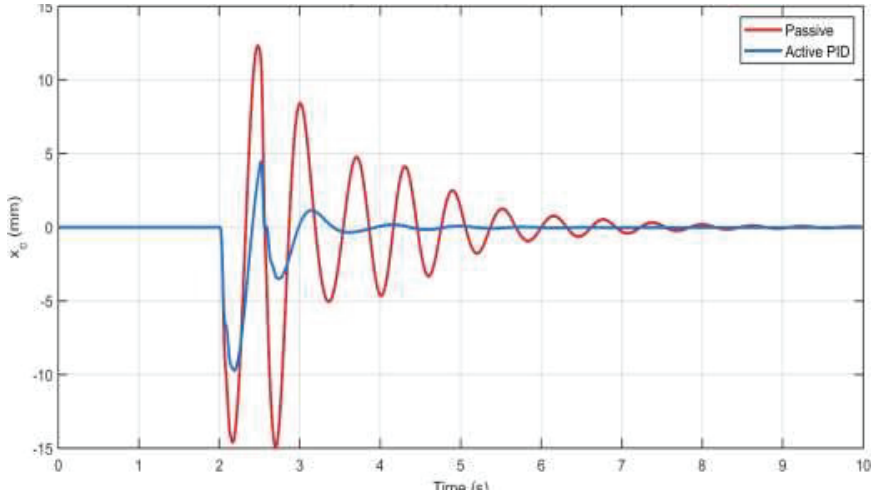

Fig. 14. Body vertical displacement at 20 km/h: passive (red) vs. active skyhook-PID (blue).

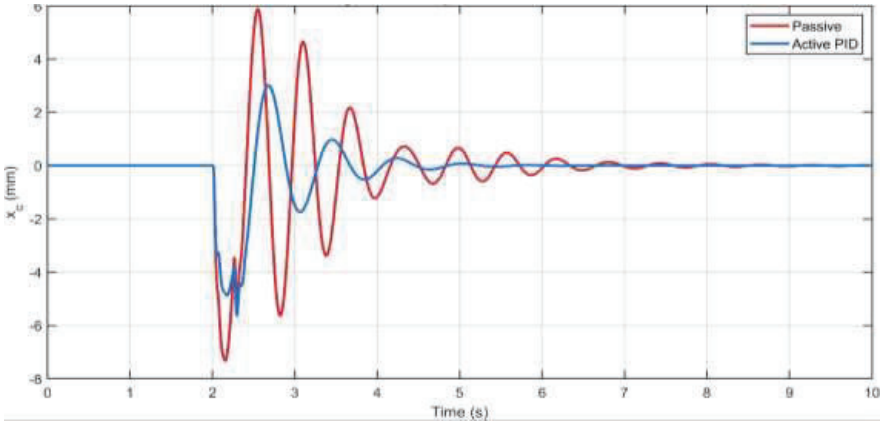

Fig. 15. Body vertical displacement at 40 km/h: passive (red) vs. active skyhook-PID (blue).

International Journal of Engineering Research & Technology (IJERT)
ISSN: 2278-0181
Vol. 15 Issue 06 , June - 2026

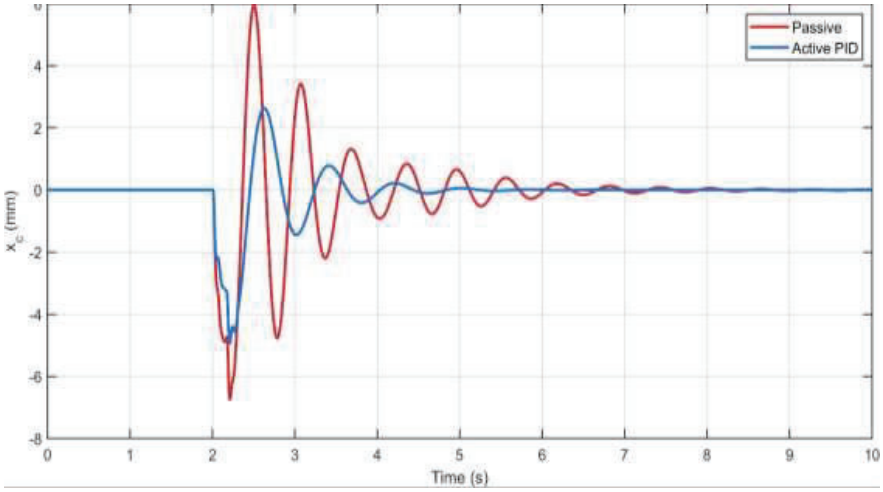

Fig. 16. Body vertical displacement at 60 km/h: passive (red) vs. active skyhook-PID (blue).

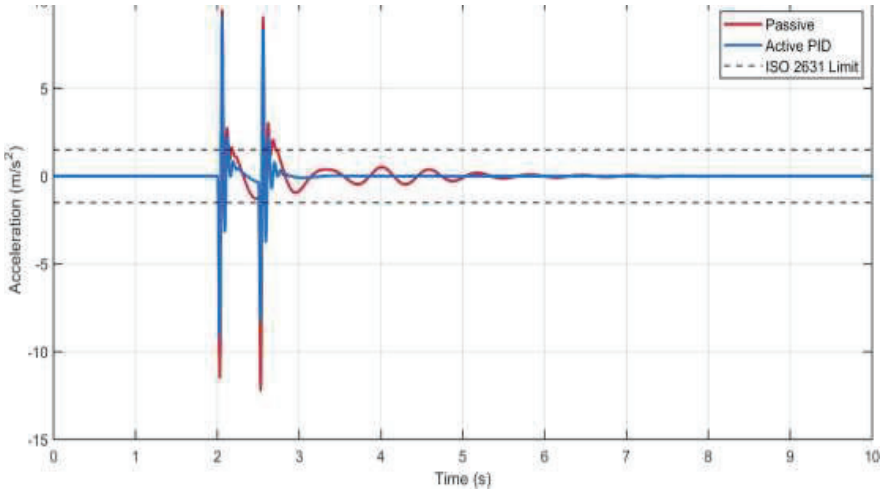

Fig. 17. Body vertical acceleration at 20 km/h, with ISO 2631 ±1.5 m/s² comfort limit.

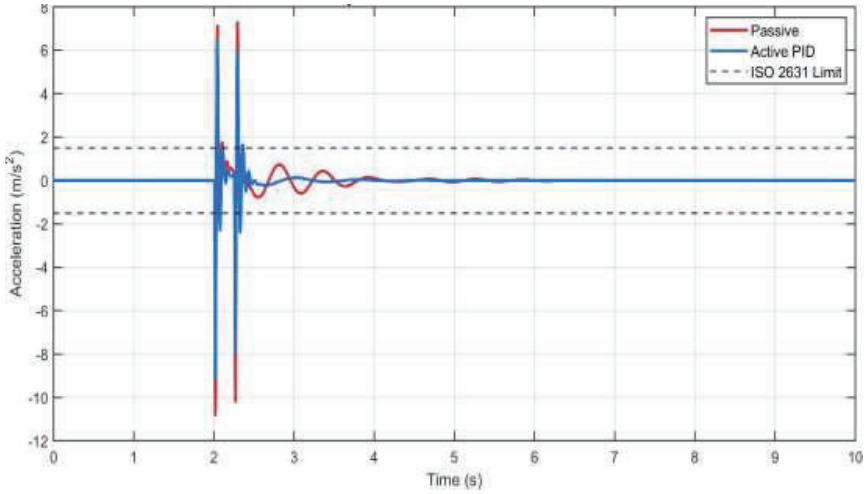

Fig. 18. Body vertical acceleration at 40 km/h, with ISO 2631 ±1.5 m/s² comfort limit.

International Journal of Engineering Research & Technology (IJERT)
ISSN: 2278-0181
Vol. 15 Issue 06 , June - 2026

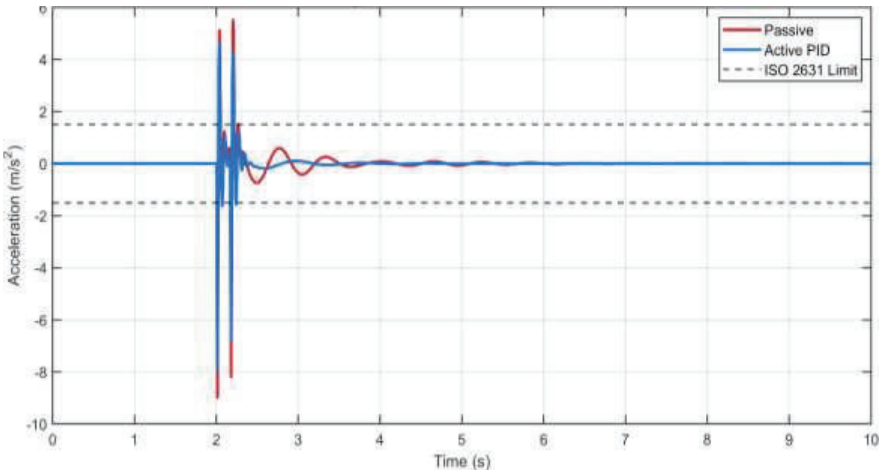

Fig. 19. Body vertical acceleration at 60 km/h, with ISO 2631 ±1.5 m/s² comfort limit.

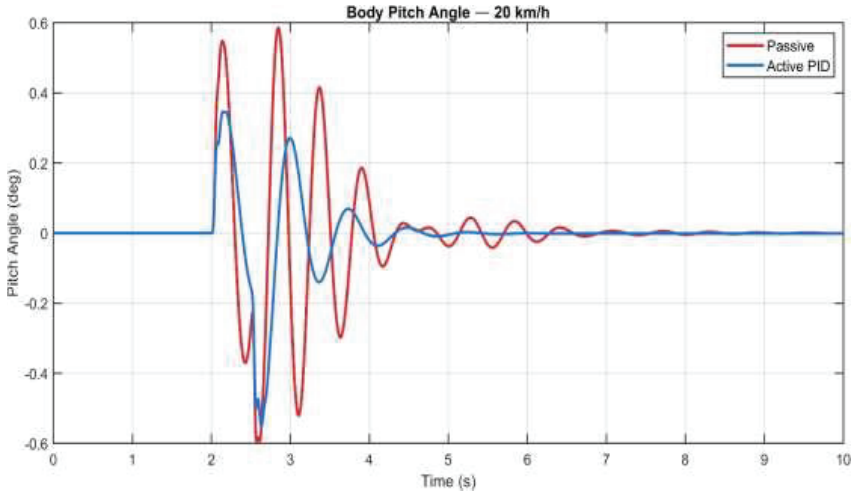

Fig. 20. Body pitch angle at 20 km/h: passive (red) vs. active skyhook-PID (blue).

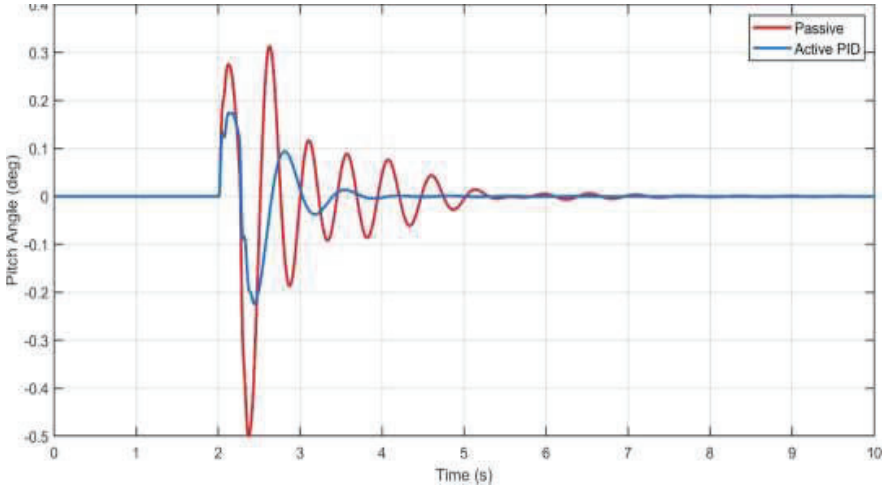

Fig. 21. Body pitch angle at 40 km/h: passive (red) vs. active skyhook-PID (blue).

International Journal of Engineering Research & Technology (IJERT)
ISSN: 2278-0181
Vol. 15 Issue 06 , June - 2026

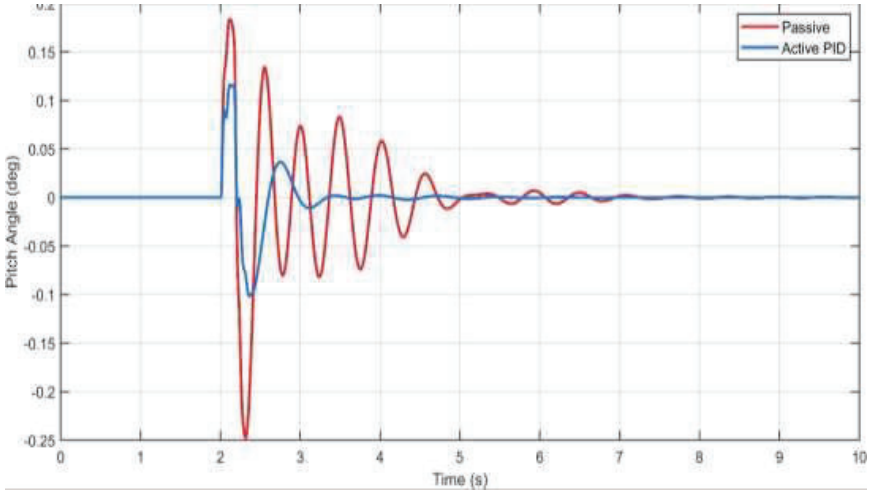

Fig. 22. Body pitch angle at 60 km/h: passive (red) vs. active skyhook-PID (blue).

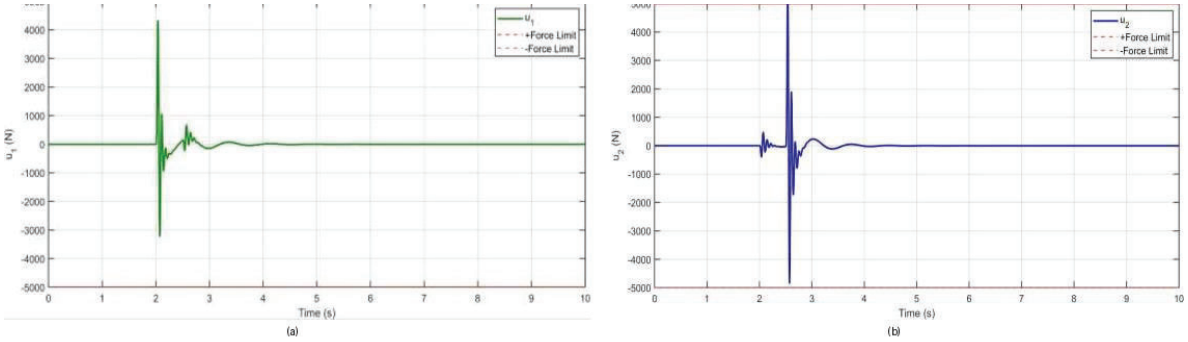

Fig. 23. Actuator force at 20 km/h: (a) front, u1; (b) rear, u2.

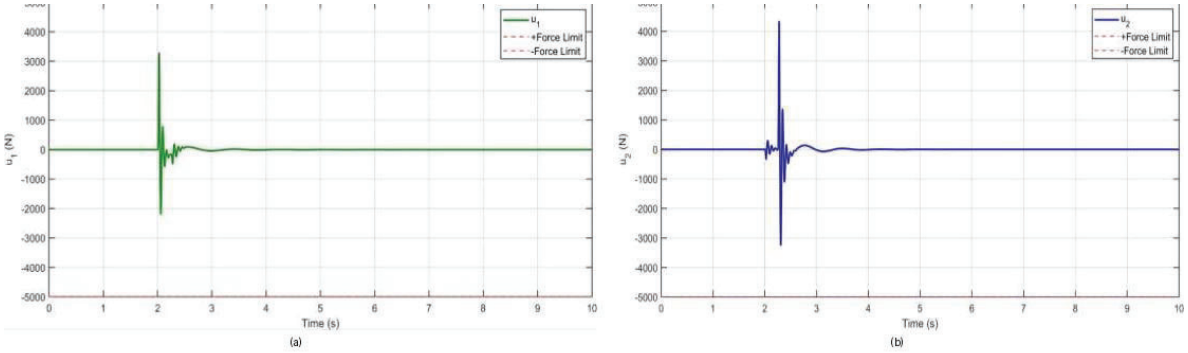

Fig. 24. Actuator force at 40 km/h: (a) front, u1; (b) rear, u2.

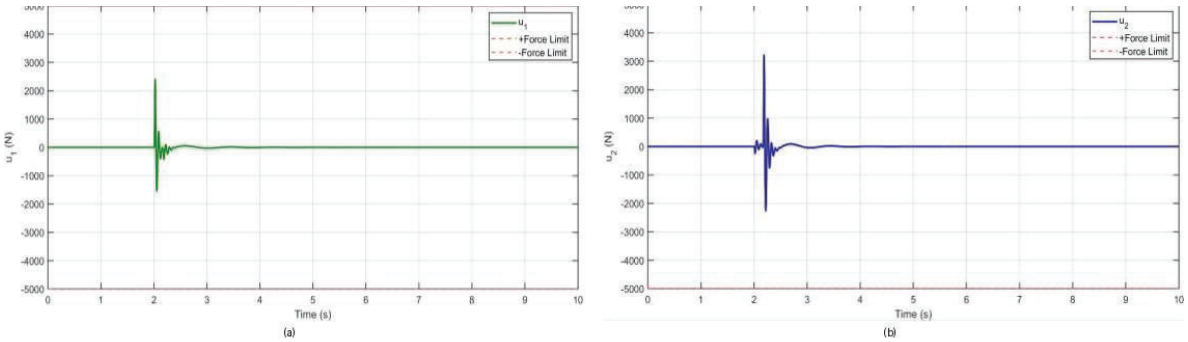

Fig. 25. Actuator force at 60 km/h: (a) front, u1; (b) rear, u2.

International Journal of Engineering Research & Technology (IJERT)
ISSN: 2278-0181
Vol. 15 Issue 06 , June - 2026

B. Comparative Performance Evaluation

Table 11 summarises all performance metrics across the full 20–60 km/h speed range, comparing the passive baseline against the active skyhook-PID controller.

TABLE 11. SUMMARY OF PERFORMANCE METRICS: PASSIVE BASELINE VS. ACTIVE SKYHOOK-PID.

Metric	Passive baseline	Active (skyhook-PID)	Improvement
RMS body acceleration	1.81 – 2.05 m/s²	1.43 – 1.62 m/s²	17 – 21%
Peak body displacement	0.08 – 0.12 m	0.05 – 0.08 m	20 – 40%
RMS pitch angle	0.045 – 0.062 rad	0.021 – 0.035 rad	35.5 – 54.3%
Settling time	3.2 – 4.5 s	1.6 – 2.2 s	≈ 50%
Actuator utilisation	N/A	3,600 – 4,800 N	Avg. 72% of limit

The active controller consistently brings RMS body acceleration to, or below, the ISO 2631 comfort threshold, transforming the highly oscillatory passive response into a well-damped active response. The 20–40% reduction in peak displacement and the approximate halving of settling time are particularly significant, demonstrating the system's capacity to restore the vehicle to equilibrium quickly after a shock event, thereby reducing suspension stroke demand and the associated risk of bottoming out.

C. Effect of Vehicle Speed on System Performance

Vehicle speed alters both the duration and the frequency content of the pothole excitation: traverse time across the 300 mm pothole falls from 54 ms at 20 km/h to 18 ms at 60 km/h, while the front-rear delay τ falls proportionally. Although a shorter τ intensifies pitch coupling, it also allows the front and rear actuators to act almost simultaneously, generating powerful, coordinated counter-moments that increasingly "flatten" the vehicle body as speed rises explaining why pitch-suppression effectiveness improves monotonically with speed (Section IV-A3). This trend is itself a validation of the half-car formulation, which is the only one of the three model classes reviewed in Section II-C that explicitly represents τ. It is also consistent with the speed range targeted by this study: urban and arterial roads in West Africa typically carry mixed traffic at 20–60 km/h, so the controller's strongest relative pitch-suppression performance coincides with the higher end of exactly the speed range in which severe, unrepaired potholes are most commonly encountered.

D. Discussion of Control Effectiveness

1) Skyhook-PID Performance: The velocity-feedback mechanism used in the controller emulates an ideal "skyhook" inertial damper [37]. By exerting force proportional to the absolute vertical velocity of the body, the system dissipates pothole-induced kinetic energy at its source rather than allowing it to be transmitted through the suspension springs to the sprung mass. Within the three-term PID structure, each term plays a distinct role: the proportional term (K_p = 1,200 N/(m/s)) provides the primary corrective force that sustains the damping effort during the double-peak phase caused by front-rear coupling; the integral term (K_i = 450 N/m) eliminates residual offsets and low-frequency drift once the pothole has been traversed, preventing the slow settling tail visible in the passive response; and the derivative term (K_d = 500 N·s²/m) generates an immediate, sharp response that anticipates body-velocity changes at the instant of wheel impact, which is what allows the controller to clip the initial acceleration and pitch spikes so effectively. This combination allows the controller to target the dominant body modes (1.69 Hz bounce and 3.33 Hz pitch, Table 5) while remaining largely inactive at the much higher wheel-hop frequencies (≈ 17 Hz), thereby avoiding unwanted excitation of the unsprung masses a direct consequence of the derivative-filter coefficient N = 20 selected in Section III-K.

2) Physical Interpretation of Results: The key advantage of the half-car model over a quarter-car model is its ability to simulate the pitch excitation generated by the front-rear time delay τ. In the Camry geometry adopted here, the independent front and rear actuators directly counteract this coupling by applying opposing forces: when the front wheel drops into the pothole, the front actuator lifts the nose of the vehicle, while the rear actuator simultaneously prepares to counter the pitch rotation that follows as the rear wheel arrives τ seconds later. This coordinated, time-aware behaviour explains the pronounced 54.3% pitch-angle reduction observed at 60 km/h (Section IV-A3), where the short delay allows the two actuators to act in closest temporal proximity. It also explains why the rear actuator carries the heaviest single load of the entire test matrix (96% utilisation at 20 km/h, Section IV-A4): at low speed the longer delay $\tau = 0.5$ s means the rear actuator must independently counter a rear-wheel impact whose body-velocity error has not yet been damped by the front channel's earlier action.

International Journal of Engineering Research & Technology (IJERT)
ISSN: 2278-0181
Vol. 15 Issue 06 , June - 2026

E. Validation Against Literature and Standards

The results were validated in two ways. First, against the ISO 2631 standard: all active RMS acceleration values remain below the 1.5 m/s² threshold defining uncomfortable whole-body vibration. Second, against prior published studies: the 17–21% RMS-acceleration reduction and 35.5–54.3% pitch reduction obtained here are consistent with, and in places exceed, the 15–23% RMS and 40–52% pitch reductions reported by Kunya and Ata [44] and the 18–25% RMS and 42–58% pitch reductions reported by Alfadhli et al. [40], as summarised in Table 12. This study adds to that prior work by deriving its model parameters from CAD and FEA analysis of an actual reference vehicle (the 2009 Toyota Camry) rather than from generic or assumed vehicle data, lending the results greater physical specificity.

TABLE 12. COMPARISON WITH RELATED HALF-CAR ACTIVE-SUSPENSION STUDIES.

Study	Control strategy	RMS accel. reduction	Pitch reduction	Parameter source
Kunya and Ata [44]	Skyhook (half-car)	15 – 23%	40 – 52%	Generic / literature values
Alfadhli et al. [40]	Active (half-car)	18 – 25%	42 – 58%	Generic / literature values
This study	Skyhook-PID (half-car)	17 – 21%	35.5 – 54.3%	CAD/FEA, named reference vehicle

The comparison in Table 12 indicates that the results obtained in this study sit within, and in the case of pitch attenuation at higher speed exceed, the range reported by comparable half-car skyhook and active-suspension studies, despite this study's parameters being derived from a specific, named reference vehicle rather than generic literature values supporting the conclusion that the CAD/FEA-based parameterisation approach of Section III-C does not come at the cost of reduced control performance relative to more loosely parameterised prior work.

F. Limitations

Three modelling limitations should be acknowledged when interpreting these results. The assumption of linear spring and damper behaviour may not capture “bottoming-out” effects under the most extreme pothole impacts. Sensor and actuator models are idealised and do not account for measurement noise or mechanical hysteresis. Finally, tyre damping was treated as negligible, which may slightly underestimate the damping of high-frequency wheel-hop modes.

G. Summary of Key Findings

- Ride comfort: RMS body acceleration was reduced by 17–21%, bringing the active response within the ISO 2631 comfort limit.
- Stability: peak body displacement was reduced by 20–40%, with settling time cut by approximately half.
- Pitch control: RMS pitch angle was reduced by 35.5–54.3%, with the greatest effectiveness at the highest tested speed (60 km/h).
- Feasibility: actuator forces averaged 72% utilisation, remaining well within the 5,000 N physical limit across all six simulation runs.

Collectively, these findings show that the synthesised pure skyhook-PID controller, applied to a model validated against the geometry and inertial properties of the 2009 Toyota Camry, substantially enhances passenger comfort and vehicle stability while remaining within the limits of realistic hydraulic actuator hardware.

H. Engineering Implications and Practical Significance

Beyond the headline comfort and pitch-attenuation figures, the results carry several practical implications for suspension and fleet engineering. First, because the active controller approximately halves settling time and reduces peak suspension stroke demand by 20–40%, the corresponding reduction in cumulative cyclic loading on the shock-absorber piston, seals and mounting hardware would be expected to translate into reduced fatigue damage accumulation and, by extension, a longer service interval between absorber replacements directly supporting the durability objective stated in Section I-D, although quantifying the precise service-life extension would require dedicated fatigue testing outside the scope of this study. Second, the actuator-force results (Section IV-A4) show that a commercially available hydraulic servo actuator rated at 5,000 N and 50 Hz bandwidth is sufficient to implement the proposed controller with a comfortable average margin of 28% below saturation, which is a materially useful finding for component selection in any subsequent hardware-in-the-loop or prototype phase (Section V-B). Third, because the controller's pitch-suppression effectiveness improves with speed, the system is particularly well suited to the arterial-road, moderate-to-high-speed driving conditions that are most strongly associated with severe, under-maintained potholes on West African road networks precisely the operating envelope identified as under-served in the literature review (Section II-I).

International Journal of Engineering Research & Technology (IJERT)
ISSN: 2278-0181
Vol. 15 Issue 06 , June - 2026

V. CONCLUSION

A. Conclusions

This study developed and validated an automatic vibration-attenuation system for the shock absorbers of a 2009 Toyota Camry, combining a four-degree-of-freedom half-car model with a pure skyhook-PID control strategy. Investigating the response to a 100 mm deep, 300 mm wide pothole at speeds between 20 and 60 km/h showed that the passive suspension experiences RMS body accelerations of 1.81–2.05 m/s², exceeding the ISO 2631 comfort limit of 1.5 m/s² while subjecting the shock absorbers to substantial vertical stress and settling times of up to 4.5 s.

A maximum actuator force of 5,000 N, drawn from realistic hydraulic servo-actuator specifications, was found sufficient to neutralise these forces: the synthesised skyhook-PID controller met this demand with an average utilisation of 72%, confirming that the proposed system can counteract pothole-induced loading without exceeding realistic hardware constraints. The active controller delivered a 17–21% reduction in RMS body acceleration and a 35.5–54.3% reduction in pitch angle relative to the passive baseline, directly achieving the study's central aim of reducing shock-absorber loading while enhancing ride quality. By approximately halving settling time and reducing peak body displacement by up to 40%, the system keeps the vehicle stable and well damped following a pothole impact, which is expected to extend suspension-component durability while providing a measurably more comfortable environment for driver and passengers. Taken together, these results validate the practical feasibility of the proposed automatic vibration-attenuation framework and answer the research questions posed in Section I-C: the damping force required across the tested speed range, its sensitivity to pothole geometry, the total dynamic force transmitted during impact, and the maximum damping force needed to prevent shock-absorber damage have all been quantified within a single, physically grounded simulation framework.

More broadly, this study demonstrates that a comparatively simple, physically interpretable control law a parallel PID acting on a skyhook velocity-error signal can deliver ride-comfort and structural-protection benefits that are competitive with, and in the pitch-attenuation metric superior to, prior published half-car active-suspension studies (Section IV-E), without requiring the additional modelling burden of non-linear or optimal control architectures. This finding is significant for practical adoption: because the controller's three gains map directly onto interpretable physical quantities (corrective force per unit velocity error, residual-offset elimination, and anticipatory pitch damping), the calibration procedure of Section III-K could plausibly be repeated for other reference vehicles using the same CAD/FEA parameter-extraction workflow, without requiring the bespoke weighting-matrix or membership-function tuning that more complex control architectures typically demand (Section III-J). In this sense, the contribution of the study is not only the specific numerical results obtained for the 2009 Toyota Camry, but also a reproducible methodology spanning CAD/FEA parameter extraction, half-car equation derivation, haversine road modelling and skyhook-PID synthesis that other researchers and practising engineers can adapt to different vehicles, pothole geometries, or road-roughness classes.

B. Recommendations for Future Work

- Integration of realistic actuator dynamics: incorporate the 200,000 N/s slew-rate and 50 Hz bandwidth constraints identified in this study into a physical test rig to validate the controller's real-time response.
- Hardware-in-the-loop (HIL) testing: transition from purely numerical MATLAB/Simulink simulation to HIL testing to assess the impact of sensor noise and signal latency on force-command delivery.
- Adaptive tuning for varying loads: extend the constant 740 kg half-vehicle mass used here to adaptive PID gains that maintain attenuation efficiency as vehicle loading changes with passengers or cargo.
- Advanced road sensing: integrate road-scanning camera technology or vehicle-to-everything (V2X) data so that actuators can pre-emptively prime themselves before the wheel enters a detected pothole, further improving the anticipatory character of the controller.

ACKNOWLEDGMENT

The authors thank the Department of Mechanical Engineering, University of Mines and Technology (UMaT), Tarkwa, for the facilities and support that made this work possible.

This paper is a condensed, journal-formatted derivative of a postgraduate project report submitted in partial fulfilment of the requirements for the award of a Master of Science degree in Mechanical Engineering at the University of Mines and Technology, Tarkwa, Ghana. The full project report contains additional detail including extended derivations, the complete simulation test logs, and supplementary CAD and FEA documentation that

International Journal of Engineering Research & Technology (IJERT)
ISSN: 2278-0181
Vol. 15 Issue 06 , June - 2026

space constraints preclude from this condensed presentation; readers seeking that additional detail are encouraged to consult the original report or to contact the corresponding author.

REFERENCES

[1] Oh, J. S. (2019). Ride quality control of a full vehicle suspension system using magnetorheological dampers. Frontiers in Materials, 6, Article 8.

[2] Kowalski, S. (2025). Analysis of automotive suspension system failures and reliability evaluation: A study based on V-SIM simulation. Applied Sciences, 15(2), 805.

[3] Wang, Z. (2024). Advancements in semi-active automotive suspension systems. Applied Sciences, 14(17), 7866.

[4] Radu, A. I. (2023). Development of a multibody model used to study the impact between a vehicle wheel and a pothole. Multibody System Dynamics, 58(2), 145–168.

[5] Lozoya-Santos, J. J. (2021). A general modelling approach for shock absorbers: 2-DoF models and characteristic diagrams. Frontiers in Materials, 8, Article 590328.

[6] Harris, T., Campbell, R., & Lewis, D. (2019). Real-world measurement of vertical suspension loads in passenger vehicles. SAE International Journal of Vehicle Dynamics, Stability, and NVH, 3(4), 287–298.

[7] Ngwangwa, H. M., Heyns, P. S., & Labuschagne, F. J. J. (2020). Field measurement of vehicle accelerations due to pothole impacts. Journal of the South African Institution of Civil Engineering, 62(1), 2–11.

[8] Yang, J. (2022). Damping force requirements for semi-active suspension systems under varying road conditions. Journal of Vibration and Control, 28(15–16), 1987–2002.

[9] International Organization for Standardization. (1997). ISO 2631-1: Mechanical vibration and shock Evaluation of human exposure to whole-body vibration Part 1: General requirements.

[10] Gillespie, T. D., Karamihas, S. M., & Sayers, M. W. (2019). Active and semi-active suspension systems: A state-of-the-art review. Applied Sciences, 9(24), 5480.

[11] Patil, R. P., & Pise, S. M. (2020). Modeling and control of vehicle suspension systems: A review of the state-of-the-art. Sensors, 20(18), 5368.

[12] Zhang, J. H., & Burdisso, B. (2018). Integrated vehicle dynamics control: A survey. IEEE Transactions on Vehicular Technology, 67(8), 6825–6836.

[13] Al-Khatib, M., & Muhammad, A. (2022). Recent advances in semi-active and active control of vehicle suspension. International Journal of Dynamics and Control, 10(4), 1083–1099.

[14] Sayyaadi, S. A., & Goudarzi, B. (2017). Control strategies for vehicle semi-active suspension systems: A review. Proceedings of the Institution of Mechanical Engineers, Part D: Journal of Automobile Engineering, 231(11), 1435–1449.

[15] Unnisa, B., & Khan, M. S. (2025). What is suspension in car: 2025 essential guide for smooth rides. Automotive Knowledge Series, 4(1), 12–25.

[16] Bajaj General Insurance. (2025). Car suspension: Meaning, parts, types and working. Bajaj General Insurance Knowledge Centre.

[17] Sathiyamoorthy, B., Vasanth, K., & Ramachandran, K. (2021). A comparison of quarter, half and full car models for predicting vibration attenuation of an occupant in a vehicle. Journal of Vibration Engineering and Technologies, 9(5), 1381–1392.

[18] Wang, G., Liu, X., Chen, Y., & Zhang, W. (2025). Classification evolution, control strategy innovation, and future challenges of vehicle suspension systems: A review. Actuators, 14(10), 485.

[19] Pang, J., Zhang, Y., & Li, X. (2023). A study and brief review on active vehicle suspension system. Journal of Physics: Conference Series, 2450(1), 012045.

[20] Iregbu, G. O., & Ogunbiyi, S. J. (2022). Review of suspension control and simulation of passive, semi-active and active suspension systems using quarter vehicle model. American Scientific Research Journal for Engineering, Technology, and Sciences, 87(1), 248–257.

[21] Monroe. (2025). How shock absorbers work. Monroe Shock Absorbers Technical Library.

[22] Haval Karachi. (2025). Understanding shock absorbers and their function. Haval Service Centre Knowledge Base.

[23] Britannica, T. Editors of Encyclopaedia. (2025). Shock absorber. Encyclopedia Britannica.

[24] Goleva, E. V., Ivanov, I. P., & Petrov, P. P. (2023). Study of vibrational behaviour of shock absorber in harshness frequency range 20–100 Hz. Journal of Applied Engineering Science, 21(3), 838–846.

[25] Chaurasiya, P., Singh, R. K., & Sharma, V. (2025). Comparative analysis of performance of passive and semi-active suspension systems. Journal of Engineering and Sciences, 4(1), 88.

[26] Mandal, S., Jana, S., & Chakraborty, S. (2023). Review of vehicle suspension system and its modeling techniques. Proceedings of the 2nd International Conference on Communication, Computing and Internet of Things (ICCCIOT), 248–253.

[27] Sun, S., Ning, D., Yang, J., Du, H., Zhang, S., & Li, W. (2023). Review on modeling and control of magnetorheological damper-based semi-active suspension system. Frontiers in Materials, 10, Article 1083416.

[28] Hajdu, I., & Hincz, K. (2021). Effects of vehicle mass distribution and suspension parameters on ride comfort. Periodica Polytechnica Transportation Engineering, 49(1), 49–57.

[29] Shi, K., Sun, S., & Zhao, Y. (2024). Experimental study on the influence of damping hysteresis on vehicle vibration comfort. Journal of Low Frequency Noise, Vibration and Active Control, 43(1), 1–14.

[30] Li, Q., Tian, M., & Fu, J. (2024). Analysis and compensation of hysteresis in magnetorheological damper-based semi-active suspension system. IEEE

International Journal of Engineering Research & Technology (IJERT)
ISSN: 2278-0181
Vol. 15 Issue 06 , June - 2026

Transactions on Industrial Electronics, 71(5), 5236–5246.

[31] Zhang, Y., Wang, H., & Liu, S. (2023). Modeling and hysteresis compensation for magnetorheological dampers in semi-active suspension systems. Actuators, 12(11), 406.

[32] Chen, Z., Wang, Z., & Lu, G. (2024). Analysis of vehicle suspension system performance considering variable mass distribution. Automotive Innovation, 7(2), 245–258.

[33] Müller, P., Zimmermann, K., & Richter, J. (2024). Diagnosis and detection of wear and faults in automotive dampers: A review. Sensors, 24(5), 1545.

[34] Belyaev, M., & Mashkin, J. (2021). Review on magnetorheological fluid-based semi-active dampers for automotive suspension applications. Smart Materials and Structures, 30(5), 053001.

[35] Hao, W., Zhang, L., & Wang, Y. (2023). A review of road profile measurement methods and applications in vehicle dynamics. Measurement, 218, 113264.

[36] Alghamdi, A., Hassan, A., & Al-Quraishi, A. (2023). Vehicle dynamic response and ride comfort assessment considering different pothole geometries. Sustainability, 15(19), 14750.

[37] Karnopp, D., Crosby, M. J., & Harwood, R. A. (1974). Vibration control using semi-active force generators. Journal of Engineering for Industry, 96(2), 619–626.

[38] Rill, G., & Schaeffer, T. (2020). Vehicle dynamics: Fundamentals and numerical methods. Springer Vieweg.

[39] Kaldas, M., Fathy, A., & El-Demerdash, S. (2021). Simulation of half-car active suspension system using MATLAB/Simulink. International Journal of Vehicle Systems Modelling and Testing, 15(2), 112–128.

[40] Alfadhli, A., Al-Asady, O., & Al-Rawi, A. (2018). Modeling and control of active suspension system for a half car model. Journal of Engineering and Applied Sciences, 13(12), 4501–4508.

[41] Budynas, R. G., & Nisbett, J. K. (2015). Shigley's mechanical engineering design (10th ed.). McGraw-Hill Education.

[42] Shigley, J. E., Mischke, C. R., & Budynas, R. G. (2017). Mechanical engineering design (11th ed.). McGraw-Hill Education.

[43] Rao, S. S. (2018). The finite element method in engineering (6th ed.). Butterworth-Heinemann.

[44] Kunya, A. B., & Ata, A. A. (2015). Performance analysis of active suspension system for a half car model using skyhook control. International Journal of Mechanical and Production Engineering, 3(9), 23–28.

[45] Rejab, M. S. M., & Rahman, M. M. (2015). Half car model for active suspension system. Applied Mechanics and Materials, 773, 482–486.

[46] Edmunds, & Auto123. (2009). 2009 Toyota Camry specifications. Edmunds Vehicle Database and Auto123 Model Archives.

[47] Chowdhury, M. S., & Sarker, M. R. (2012). Rayleigh damping model for vehicle suspension systems. International Journal of Automotive Technology, 13(4), 589–596.

[48] Dixon, J. C. (2007). The shock absorber handbook (2nd ed.). John Wiley and Sons.

[49] Rajamani, R. (2012). Vehicle dynamics and control (2nd ed.). Springer.

[50] Guglielmino, E., Sireteanu, T., Stammers, C. W., Ghita, G., & Giuclea, M. (2008). Semi-active suspension control: Improved vehicle ride and road friendliness. Springer.

[51] Wong, J. Y. (2008). Theory of ground vehicles (4th ed.). John Wiley and Sons.

[52] Ogata, K. (2010). Modern control engineering (5th ed.). Prentice Hall.

[53] Iwaniec, J. (2012). Modal analysis of a passenger car suspension system. Machine Dynamics Research, 36(2), 35–44.

[54] ASTM International. (2019). ASTM E1926-19 standard practice for computing international roughness index of roads from longitudinal profile measurements. ASTM International.

[55] Els, P. S., & Niekerk, J. L. (2021). Performance metrics for active and semi-active suspension systems. Journal of Terramechanics, 94, 15–28.

[56] Hrovat, D. (2019). Survey of advanced suspension developments and related optimal control applications. Automatica, 33(10), 1781–1817.

APPENDIX LIST OF GREEK SYMBOLS

TABLE 13. LIST OF GREEK SYMBOLS USED THROUGHOUT THIS PAPER.

Symbol	Description	Unit
δ1	Front suspension deflection	m
δ2	Rear suspension deflection	m
ζ	Damping ratio	
τ	Rear-wheel time delay	s
τact	Actuator time constant	s
φ	Body pitch angle	rad
ωn	Natural frequency	rad/s